Chemical Engineering Journal 460 (2023) 141631

Contents lists available at ScienceDirect

Chemical Engineering Journal

journal homepage: www.elsevier.com/locate/cej

Loading and co-solvent-triggered release of okanin, a C_4 plant key enzyme inhibitor, into/from functional microgels

Jonas Dittrich [a,b,1,2], Fabian Kolodzy [a,c,d,1,3], Alexander Töpel [a,c,d,4], Alexander Hofmann [a,e,5], Georg Groth [a,e,6], Andrij Pich [a,c,d,f,7,*], Holger Gohlke [a,b,g,*,8]

[a] Bioeconomy Science Center (BioSC), Forschungszentrum Jülich, 52425 Jülich, Germany
[b] Institute for Pharmaceutical and Medicinal Chemistry, Heinrich Heine University Düsseldorf, 40225 Düsseldorf, Germany
[c] DWI-Leibniz-Institute for Interactive Materials, RWTH Aachen University, 52056 Aachen, Germany
[d] Institute of Technical and Macromolecular Chemistry, RWTH Aachen University, 52074 Aachen, Germany
[e] Institute of Biochemical Plant Physiology, Heinrich Heine University Düsseldorf, 40225 Düsseldorf, Germany
[f] Aachen Maastricht Institute for Biobased Materials, Maastricht University, Geleen 6167 RD, Netherlands
[g] John von Neumann Institute for Computing (NIC), Jülich Supercomputing Centre (JSC), and Institute of Bio- and Geosciences (IBG-4: Bioinformatics), Forschungszentrum Jülich GmbH, 52425 Jülich, Germany

ARTICLE INFO

Keywords:
Microgel carrier
All-atom molecular dynamics simulations
Herbicide
Free energy

ABSTRACT

The constantly growing world population leads to increasing demands for food, which challenges modern agriculture manifold. Pests, such as weeds, require the application of agrochemicals to increase crop yield. Due to the environmental impact of these potentially hazardous chemicals, the demand for more efficient formulations is increasing. Promising formulations consist of easily adaptable carriers from which controllable stimuli release the agrochemicals. Here, we investigated poly(*N*–vinylcaprolactam) (pVCL)-based microgels as a potential carrier for okanin, an inhibitor of the C_4 plant key enzyme phosphoenolpyruvate carboxylase, by combining experiments, molecular simulations, and free energy computations. Dynamic light scattering, scanning transmission electron and atomic force microscopy revealed that pVCL microgels collapse and rigidify upon the loading of okanin. The simulations identified loosely adsorbed okanin and tightly bound okanin mediating interchain crosslinks. With increasing okanin concentration, stacking interactions of okanin occur with adsorbed and bound okanin. These findings can explain the experimentally observed collapse and the rigidification of the microgels. Based on the atomistic insights, two poly(*N*–vinylcaprolactam–*co*–glycidyl methacrylate) microgels were synthesized, for which a doubled loading capacity of okanin was found. Finally, we investigated the triggered release of okanin using the addition of green solvents as a stimulus both *in vitro* and *in planta*. This work establishes a basis for the further optimization of pVCL-based microgels as a carrier for the delivery of polyphenolic agrochemicals.

1. Introduction

Sustainable agriculture is of vital importance considering the growing world population. Crop productivity can be significantly increased by the use of fertilizers and pesticides [1]. However, wash off by rain, or spray drifts of the applied agrochemicals lead to a reduction

* Corresponding authors at: Forckenbeckstr. 50, 52056 Aachen, Germany, (Andrij Pich); Universitätsstr. 1, 40225 Düsseldorf, Germany, (Holger Gohlke).
E-mail addresses: pich@dwi.rwth-aachen.de (A. Pich), gohlke@uni-duesseldorf.de (H. Gohlke).
[1] These authors contributed equally.
[2] Orcid: 0000-0003-2377-2268
[3] Orcid: 0000-0002-0311-0913
[4] Orcid: 0000-0002-6801-2222
[5] Orcid: 0000-0001-8417-6748
[6] Orcid: 0000-0002-1806-9861
[7] Orcid: 0000-0003-1825-7798
[8] Orcid: 0000-0001-8613-1447

https://doi.org/10.1016/j.cej.2023.141631
Received 1 December 2022; Received in revised form 25 January 2023; Accepted 28 January 2023
Available online 31 January 2023

of the applied amount of active ingredients [2,3]. Consecutively, the applied chemicals accumulate in the soil and groundwater, posing serious health risks for humans and animals. Therefore, reducing the environmental impact of hazardous chemicals is one of the most important challenges of modern sustainable agriculture. It can be addressed by either replacing chemicals with ecologically friendly alternatives or their encapsulation to ensure a long-term release or release-on-demand mechanism triggered by a specific stimulus [4,5].

Different pathogens and pests are estimated to yield losses of up to 40 % [6]. Without adequate protection, losses potentially rise to 80 % [7]. Among all pests, weeds are possibly responsible for the highest loss [7]. Weeds are a major threat to global food production due to a rapid formation of resistance against commonly used herbicides. Hence, the constant development of novel herbicides is necessary. Chalcones are promising lead structures for the development of C_4 plant selective herbicides [8–10]. The natural polyphenolic compound okanin (2',3,3',4,4'–Pentahydroxy-chalcone) was shown to be an efficient inhibitor of phosphoenolpyruvate carboxylase, a key enzyme for carbon fixation and biomass increase in the C_4 photosynthetic pathway of many of the world's most damaging weeds [8,11].

Microgels are crosslinked, macromolecular, porous colloids, usually showing high softness and deformability. In solution, many common microgels form stable dispersions and show a stimuli-responsive swelling [12,13]. The stimuli-responsiveness can be exploited for the controlled uptake and release of different substances by using triggers such as temperature [14,15], pH [16], and different solvents. A targeted release can be achieved by tailoring the responsiveness to these triggers. Recently, microgels have attracted attention as a versatile carrier and release system for metal ions [17], small molecules [14,18–21], biomacromolecules [22–24], and even cells [25]. Many common monomers such as *N*–vinylcaprolactam (VCL) are suited for biological and medical applications due to the biocompatibility of the formed microgels [26]. Poly(*N*–vinylcaprolactam) (pVCL) is used for tissue engineering [27] and drug delivery [14,18,19] as the lower critical solution temperature (LCST) is close to the human body temperature (~32 °C in water) [28]. Polymer chains can be crosslinked either by forming new covalent bonds, e.g., with bifunctional monomers such as *N*,*N*'–methylenbis (acrylamide) (BIS), or by exploiting strong non-covalent interactions [29–31]. The latter is especially suited for the synthesis of degradable microgels, e.g., microgels crosslinked with the polyphenolic tannic acid, which degrade at basic conditions due to deprotonation of the hydroxy groups [30,31]. Reactive co-monomers such as glycidyl methacrylate (GMA) can be utilized for post-polymerization modification via the addition of nucleophiles to the epoxy group [32,33]. pVCL-based microgels with a GMA-rich shell provide access to specific surface functionalization [34]. For the use of microgels in plant protection, the stimuli-responsiveness enables release as needed so agrochemicals can be retained over a longer period. This results in fewer applications per harvesting season and, thus, reduced operating costs, while simultaneously reducing the ecological footprint [35,36]. Furthermore, microgels can be modified to increase their adhesion to leaves and improve their rain-fastness. Anchor peptides, i.e., small peptides that bind to the wax layer of the plant leaves [37], were successfully used to increase the rain-fastness of pesticide formulations. Microgels functionalized with anchor peptides were successfully used for the foliar fertilization of cucumber plants with Fe^{3+}-ions [17].

pVCL interacts with polyphenolic moieties, as shown in the supramolecular crosslinking of pVCL with tannic acid by hydrogen bonds [30]. Thus, pVCL-based microgels should be promising candidates for binding okanin. However, a pH-triggered release of okanin from the carrier is unsuited as the resulting salt stress leads to a reduction in crop yield and quality [38,39]. Green solvents [40,41], which are environmentally compatible and authorized as additives in agricultural applications, provide a suitable alternative.

In this work, we investigate pVCL-based microgels as a potential carrier for the C_4 plant key enzyme inhibitor okanin, which could lead to an aqueous formulation with increased okanin loading and/or a long-term release or a release-on-demand mechanism. In an interdisciplinary approach, we combined experiments and molecular simulations to investigate the loading of okanin into pVCL-based microgels, elucidate the binding mode, and scrutinize the co-solvent-triggered release. In more detail, we investigated the uptake of okanin into pure pVCL-based microgels under laboratory conditions using UV/Vis spectroscopy. Changes in the microgels' size upon okanin loading were traced via dynamic light scattering (DLS), and changes in the microgels' morphology were investigated using scanning transmission electron (STEM) and atomic force microscopy (AFM). Next, using all-atom molecular dynamics (MD) simulations of the uptake of okanin into the pVCL-based microgels, we obtained insights into the binding mode at the atomistic level. To improve the loading capacity of the microgel, we investigated the type of interaction between okanin and pVCL. Based on the simulation results, we incorporated glycidyl methacrylate (GMA) in both the core and shell of the pVCL microgels to increase the overall loading of okanin. Finally, we combined experimental and computational methods to analyze the co-solvent triggered release of okanin from microgels.

2. Materials and methods

2.1. Materials

N-Vinylcaprolactam (VCL, TCI, > 98,0%) was distilled and recrystallized from *n*–hexane. Glycidyl methacrylate (GMA, Sigma-Aldrich, 97 %) was distilled before use. 2,2′–Azobis(2-methylpropionamidine) dihydrochloride (AMPA, Sigma-Aldrich, 97 %), *N*,*N*'–methylenbis (acrylamide) (BIS, Sigma-Aldrich, 99 %), acetic acid (AcOH, Sigma-Aldrich, ≥ 99.0 %), dimethyl sulfoxide (DMSO, Sigma-Aldrich, ≥ 99.0 %), ethyl acetate (EtOAc, VWR Chemicals, 99.0 %), and water (H_2O, Merck-Millipore, LC-MS-grade) were used without further purification.

2.2. UV/Vis spectroscopy

UV/Vis spectra were measured with a Jasco V-780 UV–Visible/NIR spectrophotometer equipped with the USE-753 cuvette holder in the range of 300 nm to 800 nm in steps of 0.5 nm and a scanning speed of 400 nm min^{-1}. Samples in an aqueous solution were measured in polystyrene cuvettes against ultra-pure water. Samples in DMSO were measured in Quartz SUPRASIL cuvettes from Hellma Analytics against DMSO. The optical path length of all cuvettes was 1.0 cm. To obtain maximum absorbance < 1.1, samples were diluted accordingly for all measurements.

2.3. Dynamic light scattering

Dynamic light scattering (DLS) was measured at 20 °C and 50 °C with a Zetasizer Nano ZS from Malvern, operating a laser at 632.8 nm with a power of 4 mW. The scattering angle was fixed to $\Phi = 173°$. Sample dispersions were prepared in ultra-pure water and measured in polystyrene cuvettes. The concentrations of the stock solutions of unloaded microgels are described in the Supplemental Materials and Methods. For unloaded microgels, 5 µL of the microgel stock solution were added to 1200 µL of ultra-pure water ($c_{DLS,\ sample} = \sim 50\ \mu g\ mL^{-1}$). For okanin-loaded microgels ($c_{stock} = 1\ mg\ mL^{-1}$), 36 µL of the microgel stock solution were added to 1200 µL of ultra-pure water ($c_{DLS,\ sample} = \sim 30\ \mu g\ mL^{-1}$). A lower concentration for okanin-loaded microgels was chosen to account for the increased turbidity. Before each measurement, the temperature of the sample was equilibrated for 3 min. Measurements were repeated three times for each sample.

2.4. Raman spectroscopy

Raman spectra were measured on an RFS 100/s Raman spectrometer by Bruker with a Nd:YAG laser ($\lambda = 1064$ nm) with a spectral resolution of 4 cm^{-1}, a power of 200 mW, and 1000 scans in the range of 4000 cm^{-1} to 300 cm^{-1}. Samples were pressed into an aluminum pan before measurement. All spectra were baseline-corrected and normalized to the maximum if not stated otherwise.

2.5. Atomic force microscopy

Atomic force microscopy (AFM) was performed using a Veeco Instruments Nanoscope V microscope. An NCH POINTPROBE-Silicon SPM-sensor from NanoWorld, with a resonance frequency of 320 kHz, and a force constant of 42 N m^{-1} was used as the cantilever. Images were recorded in tapping mode and analyzed with the software Gwyddion [42] (v. 2.51). Before use, silicon wafers were washed with toluene, dried with nitrogen, and activated with a Flecto10USB-MFC plasma etcher (Plasma Technology) with an air plasma at 0.2 mbar and a power of 100 W for 180 s. The coating was achieved by spin coating 50 µL of the microgel dispersion (1.0 mg mL^{-1}) on the activated wafer at 2000 rpm for 60 s with a WS-650SZ-6NPP/LITE spin coater by Laurell.

2.6. Scanning transmission electron microscopy

Scanning transmission electron microscopy (STEM) measurements were performed on an Ultra-high Resolution Scanning Electron Microscope SU9000 (Hitachi-High Technologies America, Inc.) operating at a voltage of 30 kV. Therefore, 20 µL of a diluted microgel dispersion (0.1 g L^{-1}) were dropped on a TEM-grid (Carbon Film 200 Mesh Copper Grids, Electron Microscopy Sciences) and dried at room temperature overnight. All samples were sputtered with 2 nm carbon before the analysis. Images were analyzed with the software ImageJ [43].

2.7. Microgel synthesis and characterization

All pVCL-based microgels were synthesized by precipitation polymerization [32–34] with 10.538 mmol of monomers in 100 mL of ultra-pure water. The amount of VCL was 97.4 mol% (1428.6 mg, 10.264 mmol) for pure pVCL and 87.4 mol% (1282.0 mg, 9.210 mmol) for p(VCL-*co*-GMA). The amount of GMA in p(VCL-*co*-GMA) was 10.0 mol% (149.8 mg, 144 µL, 1.054 mmol, 10.0 mol%). 0.6 mol% AMPA (17.1 mg, 63 µmol) were used as the initiator and 2.0 mol% BIS (32.5 mg, 211 µmol) as the crosslinker. The composition of the microgels is summarized in Table S1.

The enrichment of GMA in the core (p(VCL/GMA_{core})) was achieved in a batch reaction according to Häntzschel et al. due to the higher reactivity of GMA compared to VCL [32–33]. A GMA-rich shell (p(VCL/GMA_{shell})) was obtained using a semi-batch approach with delayed addition of GMA as done in previous studies [34]. The GMA content of the lyophilized microgels was determined using Raman spectroscopy following an established procedure and was determined with 9.8 mol% and 10.7 mol% for p(VCL/GMA_{core}) and p(VCL/GMA_{shell}), respectively [34]. The Raman spectra are depicted in Fig. S1. The microgels' morphology was investigated by AFM and STEM. The hydrodynamic radius (R_H) and the polydispersity index (PDI) as well as the volume phase transition temperature (VPTT) were determined by DLS. The temperature-dependent results for R_H as well as the results for the VPTT are depicted in Fig. S2. More details on the microgel synthesis, the quantification of the GMA content by Raman spectroscopy, and the confirmation of the thermoresponsive properties are provided in the Supplemental Materials and Methods.

2.8. Loading of microgels with okanin

The okanin loading was investigated for pVCL, p(VCL/GMA_{shell}), and p(VCL/GMA_{core}). The workflow for the loading and purification process is depicted in Fig. 1A. A microgel stock solution (13.69 mg mL^{-1}, 17.47 mg mL^{-1} and 13.42 mg mL^{-1} for pVCL, p(VCL/GMA_{core}), and p(VCL/GMA_{shell}), respectively) was used to prepare 2000 µL of a diluted microgel dispersion (1.0 mg mL^{-1}) in 2 mL centrifuge tubes. Okanin dissolved in DMSO was added to the microgel dispersions to obtain okanin concentrations of 0.014 mM, 0.05 mM, 0.1 mM, 0.5 mM, 1.0 mM, 1.3 mM, and 2.0 mM. DMSO was added so that the total volume of DMSO in each sample was 48 µL (2.4 vol-%). For the microgels, these okanin concentrations correspond to a molar ratio n_{okanin}/n_{CU} of 0.002, 0.007, 0.014, 0.070, 0.139, 0.181, and 0.278, respectively, where n_{okanin} is the amount of okanin and n_{CU} is the number of the constitutional units (CU). The samples were mixed for 3 h. Quartz Crystal Microbalance with Dissipation monitoring (QCM-D, see Supplemental Material and Methods) experiments confirm the completion of the uptake within this time (Fig. S3). Afterward, the dispersions were centrifuged for 5 min at 43 rcf (relative centrifugal force), and 1000 µL of the supernatant was taken for further purification. The microgel dispersion was centrifuged for 20 min at 6708 rcf, the supernatant was removed, and the microgel dispersion was re-dispersed in ultra-pure water. This step was repeated thrice. All loading experiments were done as triplicates. R_H and PDI of the loaded microgels were determined by DLS. Additionally, AFM and STEM were applied to determine the radius of the width (R_{AFM}, R_{STEM}) and the height (H_{AFM}) of the microgels.

2.9. Determination of the attenuation coefficient

Due to the low solubility, a stock solution of okanin could not be prepared in ultra-pure water. Thus, the attenuation coefficient was determined in a 2.4 vol-% DMSO/water solution. For the first sample, an okanin stock solution in DMSO ($c_{stock} = 1.332$ mM) was prepared and 60 µL of the stock solution were added to 2500 µL of ultra-pure water such that the final okanin concentration was 31.22 µM. After measurement of the UV/Vis spectrum, 1280 µL of the solution were diluted in 1280 µL of a 2.4 vol-% DMSO/water solution to obtain an okanin concentration of 15.61 µM. This dilution series was continued for concentrations of 7.81 µM, 3.92 µM, 1.94 µM, and 0.97 µM. The dilution series was prepared and measured in triplicates. The UV/Vis spectra are depicted in Fig. S4. The average of the maximum absorbance at 377 nm for each point was calculated (Table S2) and plotted against the okanin concentration (Fig. S5). The attenuation coefficient ε is equal to the slope of the linear fit ($\varepsilon_{377\ nm} = (3126 \pm 14) \cdot 10^1$ L mol^{-1} cm^{-1}). ε was determined in pure DMSO as the absorption maximum exhibits a bathochromic shift ($\varepsilon_{392\ nm} = (3279 \pm 17) \cdot 10^1$ L mol^{-1} cm^{-1}), which is also observed for the binding of okanin to the microgels (Fig. S6). The corresponding UV/Vis spectra are depicted in Fig. S7 and the mean values for the maximal absorbance are listed in Table S3.

2.10. Measuring the loading of okanin into the microgel via UV/Vis

The loading of okanin into the microgels was determined by UV/Vis spectroscopy. 75 µL of the microgel stock solution ($c_{stock} = 1$ mg mL^{-1}) were added to 2500 µL of ultra-pure water ($c_{sample} = \sim 30$ µg mL^{-1}). As the turbidity of the solution depends on the initial okanin concentration (Fig. 1B), the baseline correction could not be performed using the baseline of dispersed unloaded microgels. Instead, we performed a baseline correction that is independent of the swelling state of the microgel. A comparison of different baseline correction methods revealed that an exponential baseline correction is more suited than a linear baseline correction (Fig. S8). The exponential baseline is defined as depicted in eq (1):

$$A = a \cdot e^{b \cdot \lambda} \quad (1)$$

where A is the absorbance at a certain wavelength, λ is the wavelength,

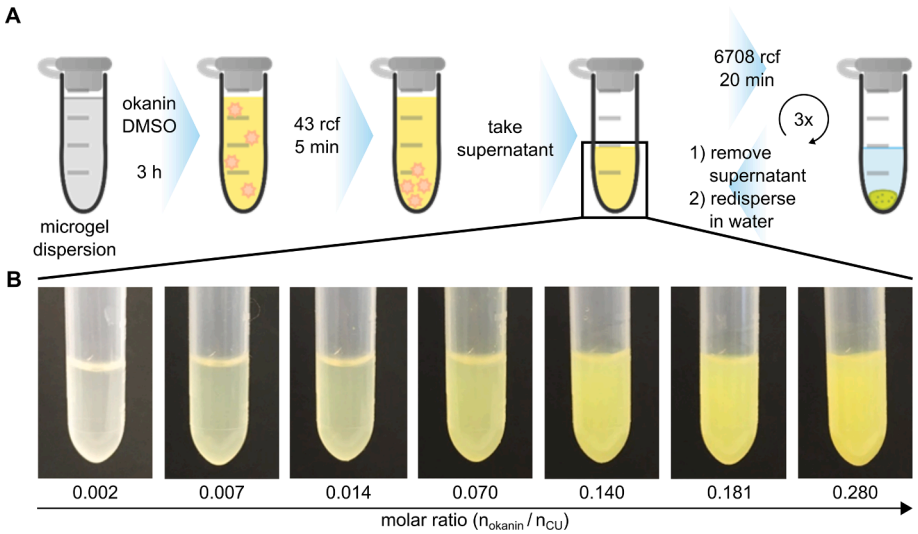

Fig. 1. Experimental workflow and exemplary images for the loading of okanin into microgels. A Schematic workflow for the okanin loading and purification of the microgels. B Images of purified pVCL microgels loaded with varying amounts of okanin in relation to the number of constitutional units (n_{okanin}/n_{CU}). Schematics in this figure were created with Chemix (https://chemix.org).

and a and b are the fitting parameters. a and b were determined for each spectrum via a two-point method for $\lambda_1 = 300$ nm and $\lambda_2 = 550$ nm according to eq (2) and eq (3), respectively.

$$b = \frac{\ln\left(\frac{A_{\lambda_1}}{A_{\lambda_2}}\right)}{\lambda_1 - \lambda_2} \tag{2}$$

$$a = \frac{A_{\lambda_2}}{e^{b \cdot \lambda_2}} \tag{3}$$

The fitting parameters a and b as well as the maximal absorbance A_{max} before and after correction are listed in the Supporting Information (Table S3 for the calibration in DMSO and Table S4–S6 for the loading of okanin into a pVCL, a p(VCL/GMA_{core}) and a p(VCL/GMA_{shell}) microgel, respectively). This correction was also applied to the calibration spectra (Fig. S7) to obtain the corrected attenuation coefficient $\varepsilon_{392nm,\,corr.} = (3176 \pm 17) \cdot 10^1$ L mol^{-1} cm^{-1} (Fig. S5).

2.11. Co-solvent-triggered release

The co-solvent-triggered release was investigated for pVCL, p(VCL/GMA_{shell}), and p(VCL/GMA_{core}) loaded at an initial okanin concentration of 0.5 mM and 1.3 mM corresponding to a molar ratio of 0.070 and 0.181, respectively. The values of initial loading are shown in Table S7–S9 for pVCL, p(VCL/GMA_{shell}), and p(VCL/GMA_{core}), respectively. 500 µL of the okanin-loaded microgel dispersion (1.0 mg mL^{-1}) were prepared in 1.5 mL centrifuge tubes. For water, DMSO, and AcOH, 50.0 µL (10.0 vol–%) of the respective co-solvent were added. In the case of EtOAc, a mixture of 47.0 µL of EtOAc (9.4 vol–%) and 3.0 µL of ultra-pure water was added due to the low solubility of EtOAc in water. The samples were mixed for 16 h. QCM-D experiments confirm the completion of the release within this time (Fig. S3). Afterward, the dispersions were centrifuged for 20 min at 6708 rcf. 400 µL of the supernatant were taken and diluted with 400 µL and 1200 µL of ultra-pure water for samples of microgels loaded at a molar ratio of 0.181 and 0.070, respectively, to determine the amount of released okanin by UV/Vis spectroscopy. All release experiments were performed in triplicates.

2.12. Computational approach

pVCL microgels often show a characteristic core–shell structure due to a gradient in crosslink density within the microgel resulting in a densely crosslinked core and less crosslinked shell [44]. To account for this core–shell structure of our microgel, we investigated the interaction of okanin with a syndiotactic linear pVCL 50mer ($M_w \approx 7{,}000$ g mol^{-1}), which represents the loosely crosslinked shell, as well as with a methyl-BIS-crosslinked cubic pVCL model with an inter-crosslink chain length of 20 repeating units ($M_w \approx 34{,}750$ g mol^{-1}), representing the densely crosslinked core (Fig. 2).

We chose the representative models based on initial tests, in which we investigated the effect of the tacticity and crosslink density on the BIS–crosslinked polymers' thermo-responsiveness by simulating three different atactic as well as one syndiotactic and one isotactic polymer cube with an inter-crosslink chain length of 20 and 40 repeating units, respectively. For each tacticity, ten replicas were simulated for 500 ns at 293 K, 313 K, and 343 K in the TIP3P [45] water model, resulting in a cumulative simulation time of 150 µs (Table S10). In line with previous experiments [46], we found a dependency of the phase transition of the pVCL model on the polymer's tacticity. Atactic and isotactic pVCL models collapse irrespective of the temperature and inter-crosslink chain length (Fig. S9 and Fig. S10). Syndiotactic pVCL showed the expected thermo-responsiveness irrespective of the inter-crosslink chain length and was selected as a model representing the core section of a pVCL microgel. To evaluate the influence of the chosen water model, we performed simulations of a crosslinked pVCL model with an inter-crosslink chain length of 20 in OPC [47] water (Table S11), resulting in a cumulative simulation time of 75 µs. In agreement with previous studies,[46] the collapse of the syndiotactic pVCL is well-defined using TIP3P water (Fig. S9 and Fig. S10), whereas the collapse is less pronounced in OPC water (Fig. S11).

To elucidate the binding mode of the herbicide okanin with the pVCL microgel carrier at an atomistic level, we employed extensive all-atom MD simulations of systems comprising linear or crosslinked pVCL with varying concentrations of okanin. We examined the influence of the okanin concentration by increasing the number of okanin molecules, going from a simulation in pure water to a molar ratio n_{okanin}/n_{CU} of 0.04, 0.14, 0.28, 0.56 to 1.11 and 0.14, 0.56 to 1.11 for the crosslinked and the linear pVCL, respectively. An overview is provided in Table S12.

To further assess the impact of okanin at different concentrations on the polymers' conformation and thermo-responsiveness, we simulated ten replicas for 1 µs each at 293 K and 313 K for each okanin concentration, yielding a cumulative simulation time of 60 µs and 120 µs for the linear and the crosslinked pVCL, respectively.

Furthermore, we investigated the effect of ethyl acetate on the pVCL

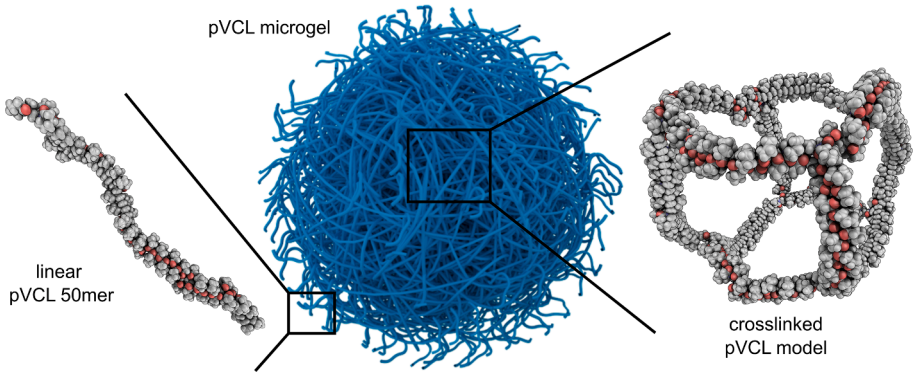

Fig. 2. Decomposition of a microgel into atomistic models for the shell and core section. Simulations of linear oligomers mimic the loosely crosslinked shell of the microgel (left); the BIS-crosslinked cubic pVCL models mimic the highly crosslinked core (right).

cube with an inter-crosslink chain length of 20 repeating units. Ethyl acetate is considered a preferred/recommended solvent [40,41] and can potentially be used to promote okanin release from the microgel. However, we note that it is not commonly used in agricultural applications and, thus, serves as an organic solvent reference and a benchmark in our study. We selected the crosslinked systems with a low (0.04) and high (0.28) initial n_{okanin}/n_{CU} and simulated each for 1 μs, yielding an additional cumulative simulation time of 80 μs for the okanin release.

2.13. Structure preparation

The generation of the parameters for the pVCL repeating unit was described in detail in our previous work [46]. For computing atomic charges, we followed the Restrained Electrostatic Potential (RESP) procedure [48]. The electrostatic potential (ESP) was calculated at the HF/6-31G* level using Gaussian09 [49]. Afterwards, the ESP was fitted using the RESP charge fitting procedure implemented in antechamber [50]. We employed the same procedure for the tetra-methylated BIS moiety and okanin. The protonation state of okanin was determined using Epik [51] within Schrödinger's Maestro [52] program, revealing a predicted pK_a value of 7.3 for the hydroxy group at position 4′ (Scheme 1), which we consider deprotonated in our simulations. For okanin, missing force field parameters were generated using the parmchk2 module of Amber20 [53]. Oligomeric pVCL and the crosslinked pVCL structures were generated using the tleap module of Amber20. The library (lib) and parameter modification (frcmod) files used are available at https://doi.org/10.25838/d5p-41. Finally, the remaining open valence of the BIS moieties within the crosslinked pVCL model and the termini of the linear pVCL oligomers were methyl-terminated. According to DLS measurements, the radius of the (swollen) microgel models is ~100-fold smaller than that of the experimental microgels.

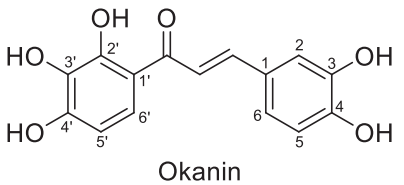

Okanin
2',3',4',3,4-Pentahydroxy-chalcone

Scheme 1. Chemical structure of okanin (2',3,3',4,4'–Pentahydroxy-chalcone). Okanin has been identified as a selective inhibitor of phosphoenolpyruvate carboxylase, a key enzyme for carbon fixation in the C_4 photosynthetic pathway of damaging weeds.[8]

2.14. Molecular dynamics simulations and analysis

MD simulations were carried out with the Amber20 suite of programs [53–54] using the GPU-accelerated version of PMEMD [55–56] by following an established procedure [46]. We applied the GAFF2 force field [57] in all simulations. The structures were solvated in a cubic box of TIP3P [45] or OPC [47] water molecules. The systems comprising different tacticity and intra-crosslink chain lengths were solvated such that the distance between the boundary of the box and the closest solute atom was at least 12 Å. For the oligomeric and crosslinked pVCL systems with a variable amount of okanin, we employed PACKMOL [58] to randomly place okanin molecules within a box comprising ~102,900 water molecules, where the box is centered at the geometric center of the pVCL model. Periodic boundary conditions were applied using the particle mesh Ewald (PME) method [59] to treat long-range electrostatic interactions. Bond lengths involving bonds to hydrogen atoms were constrained by the SHAKE [60] algorithm. The time step for all MD simulations was 2 fs, and a direct-space non-bonded cutoff of 8 Å was applied.

Geometric analyses of the trajectories were performed with pytraj [61] and CPPTRAJ [62]. To investigate the properties of pVCL interacting with okanin, we determined key characteristics such as the radius of gyration (R_g) of the pVCL and the contacts of the okanin with the pVCL. We define a contact by a distance cutoff, i.e., as any heavy atom of the okanin within 6 Å of any atom of the pVCL. Furthermore, we consider okanin with at least five contacts "adsorbed" and with > 475 contacts "bound" (see next section).

2.15. Free energy calculations

Following an established procedure [46], we estimate the binding free energy for the adsorption/binding of okanin to the pVCL microgel using the molecular mechanics Poisson-Boltzmann surface area (MM-PBSA) approach [63–66]. Therefore, we estimate the changes in the effective energy ($\Delta E_{MM} + \Delta G_{solvation}$) and approximate the changes in configurational entropy of the solutes (ΔS_{config}) upon binding using normal mode analysis [67] (NMA) as implemented in MM-PBSA.py [68]. Thus, $\Delta G_{binding}$ is defined as depicted in eq (4):

$$\Delta G_{binding} = \Delta E_{MM} + \Delta G_{solvation} - T\Delta S_{config} \quad (4)$$

E_{MM} is the sum of bonded and non-bonded molecular mechanics energies (eq (5)):

$$E_{MM} = \sum_{bonds} E_{bond} + \sum_{angles} E_{angle} + \sum_{torsions} E_{torsion} + \sum_{i\neq j}^{atoms} E_{vdW} + \sum_{i\neq j}^{atoms} E_{electrostatic} \quad (5)$$

G_{solv} denotes the solvation free energy (eq (6)):

$$G_{solv} = G_{pol} + G_{nonpol} \quad (6)$$

and changes in the configurational entropy ΔS_{config} are computed as the sum of the changes in translational, rotational, and vibrational entropy:

$$\Delta S_{config} = \Delta S_{trans} + \Delta S_{rot} + \Delta S_{vib} \quad (7)$$

G_{pol} is computed by solving the linear Poisson-Boltzmann equation [69–70] using a dielectric constant of 4 for the solute and 80 for water. G_{nonpol} is decomposed into a repulsive cavitation solvation free energy term G_{cavity} and an attractive dispersion solvation free energy term $G_{dispersion}$, which are calculated using a term linearly proportional to the molecular volume enclosed by the solvent-accessible surface area (SASA) and a surface-based integration method, respectively [71]. Finally, for the NMA, we assume that the polymer chains and the okanin molecules obey a rigid-rotor model, such that vibrational frequencies of normal modes can be calculated at local minima of the potential energy surface, and translational as well as rotational entropies can be calculated using standard statistical mechanical equations [72]. As done in previous works, for the NMA, we chose GBHCT [73–74] as a water model, and each snapshot was minimized until the convergence criterion of a difference in minimized energies between two steps of < 0.001 kcal mol^{-1} is satisfied. We note that the ΔS_{trans} (eq (7)) depends on the solute concentration [75]. Chemical equilibria that do not conserve the number of molecules, such as binding reactions, are concentration-dependent [76,77]. Here, we obtain binding free energies for a standard state of 1 M termed $\Delta G^0_{binding}$. This results in a translational entropy for each component that is smaller by 6.4 cal mol^{-1} K^{-1} than the entropy value obtained for the standard state of an ideal gas (1 atm, 298.15 K). Finally, the temperature was set to 298 K for all MM-PBSA calculations, regardless of the simulation conditions.

In total, we calculated free energies for all okanin molecules in all seven trajectories of the linear oligomer ($n_{okanin}/n_{CU} = 0.14$) where a coil-to-globule transition occurred (Fig. S12), treating the okanin molecules as independent, following the "one-trajectory approach" [68]. From the 490,000 frames in total (7 trajectories à 10,000 frames and 7 okanin molecules per system), we considered only frames where the okanin is at least adsorbed (>5 contacts) (in total 281,065 frames) for the MM-PBSA analysis. We found a dependency of $\Delta G^0_{binding}$ on the number of contacts formed with the pVCL. For the linear regression, we find a root of 475 contacts. Thus, we consider okanin molecules with $>$ 475 contacts "bound", as for these conformations, obtaining a negative $\Delta G^0_{binding}$ is more probable. The distribution of obtained $\Delta G^0_{binding}$ of bound okanin (>475 contacts, 38,824 frames) is shown in Fig. S13.

2.16. Determination of adsorbed/bound/stacked okanin species

Using contacts between the different moieties, i.e. contacts between okanin and i) the pVCL, ii) other okanin molecules, and iii) both of the aforementioned, it is possible to distinguish between different okanin species in our simulations. For okanin-polymer interactions, the determined threshold of at least 475 contacts for a potentially favorable interaction (see previous section) allows distinguishing *bound* okanin from loosely *adsorbed* okanin for low molar ratios of okanin and pVCL. For higher concentrations, however, we observe an increasing amount of stacked okanin molecules not only in aqueous solution but also onto already adsorbed or bound okanin. Thus, for higher okanin concentrations, the number of okanin molecules bound to the microgel cannot be determined solely from the contacts with the pVCL microgel but also has to include contacts with other okanin molecules. Choosing solely the same cutoff of 475 for the contacts to the microgel and other okanin molecules, however, overestimates the number of stacked okanin molecules within the microgel for higher molar ratios: To exclude okanin molecules that stack in solution, we thus require that at least 250 of the 475 contacts are formed with the pVCL for an okanin molecule to be considered *stacked within the microgel*. In an optimal stacking configuration, when both okanin molecules are parallel and the aromatic rings are placed atop each other, about ~ 250 contacts are computed for each of the involved okanin molecules. To account for possible deviations from the optimal configuration, we chose a cutoff of $>$ 200 contacts for the identification of okanin molecules involved in *stacking in solution*. Based on this classification scheme, we determined the amounts of bound and adsorbed okanin within the first layer on the microgel, okanin stacked within the microgel or in solution, and free okanin.

2.17. Quantification of okanin during release simulations in water and water/ethyl acetate

To elucidate the co-solvent-triggered release, we selected the last frames from the simulations of the crosslinked systems with an okanin/CU molar ratio of 0.04 and 0.28. All molecules within 6 Å of the pVCL microgel were kept, and all other molecules were discarded. Consecutively, the systems were re-solvated using either pure water or a saturated water/ethyl acetate solution. The resulting systems were neutralized again by adding Na^+ or Cl^- ions as needed. All okanin molecules with $>$ 475 contacts at the first frame of the release simulations are regarded as "bound" and are traced through the 1 µs-long simulations. Every okanin molecule not at least adsorbed, i.e., shows $>$ 5 contacts, for 98.9 % of the time is considered released. Therefore, the relative amount of okanin released corresponds to the number of released okanin molecules relative to the okanin molecules initially considered bound.

2.18. Co-solvent triggered release of okanin in seedling assays

Seedlings of the C_4-weed *Amaranthus retroflexus* were germinated on paper in the dark and subsequently incubated in the light for 24 h before treatment. Treatment was performed with buffer (2.4 % DMSO in water), 10 % AcOH, 9.4 % EtOAc, p(VCL/GMA_{shell}) microgels without okanin, p(VCL/GMA_{shell}) microgels saturated with okanin, p(VCL/GMA_{shell}) microgels saturated with okanin and EtOAc as a solvent-release trigger, p(VCL/GMA_{shell}) microgels saturated with okanin and AcOH as a solvent-release trigger, and a buffer solution saturated with okanin. Seedling length was measured after 2 days with n = 20 per treatment. The significance between test results was evaluated using a two-sided Mann-Whitney *U* test.

2.19. Co-solvent triggered release of okanin in leaves of adult A. retroflexus plants, measured by relative photosynthetic activity

Treatment was performed with buffer (2.4 % DMSO in water), 10 % AcOH, 9.4 % EtOAc, p(VCL/GMA_{shell}) microgels without okanin, p(VCL/GMA_{shell}) microgels saturated with okanin, p(VCL/GMA_{shell}) microgels saturated with okanin and EtOAc as a solvent-release trigger, p(VCL/GMA_{shell}) microgels saturated with okanin and AcOH as a solvent-release-trigger, and a buffer solution saturated with okanin. An area of 6 cm^2 was treated per leaf and analyzed after 5 days. Carbon Dioxide Response Curves were measured with a LiCOR6400 XT portable photosynthesis system. Photosynthetic activity before treatment was taken for reference.

3. Results and discussion

3.1. DLS, STEM, and AFM reveal that okanin triggers the collapse of the pVCL microgel and leads to a rigidification of the particle

As shown in previous works [30,31], polyphenolic compounds form strong interactions with pVCL chains, e.g., tannic acid can be used for supramolecular crosslinking of pVCL. Therefore, pVCL-based microgels depict suitable candidates for use as carriers for the herbicide okanin. To

determine the okanin loading capacity of the pVCL microgel, the initial molar ratio between okanin and the constitutional units of the microgel (n_{okanin}/n_{CU}) was varied, and the loading was determined via UV/Vis. A baseline correction of the UV/Vis spectra was performed to account for the absorbance caused by the turbidity of the microgel solution. The spectra of unloaded microgels cannot be used as a baseline since the turbidity increases with the molar ratio (Fig. 1B). As the absorbance of the microgel dispersion decreases exponentially with the wavelength, we investigated using an exponential baseline instead of a linear one (Fig. S8). We found that the exponential baseline correction (eqs (1)–(3)) yields results that are more accurate. The UV/Vis spectra before and after baseline correction are depicted in Fig. S6. The loading of the pVCL microgel in relation to the initial okanin concentration is depicted in Fig. 3A. The loading increases linearly until a molar ratio of 0.18. Between molar ratios of 0.18 and 0.28, the amount of loaded okanin remains constant at ≈ 75 µg/mg. This observation correlates with the precipitation of okanin for molar ratios above a molar ratio of 0.18 indicating the saturation of the solution. The most efficient loading is achieved at a molar ratio of 0.18 as the loading is converged.

To elucidate the impact of the amount of loaded okanin on the swelling of the microgels, R_H was determined by DLS at 20 °C ($R_{H,\,20\,°C}$) and 50 °C ($R_{H,\,50\,°C}$) depending on the initial okanin concentration (Fig. 3B). $R_{H,\,20\,°C}$ and $R_{H,\,50\,°C}$ both converge to a size of ≈ 160 nm at a molar ratio of 0.18. Independent of the temperature, fully loaded microgels are collapsed, while unloaded microgels show a temperature dependent swelling (Fig. S2). Therefore, the binding of okanin may lead to the loss of the microgel's thermo-responsiveness. Surprisingly, $R_{H,\,20\,°C}$ and $R_{H,\,50\,°C}$ do not continuously converge with increasing molar ratios. At a very low molar ratio ($n_{okanin}/n_{CU} = 0.002$), $R_{H,\,20\,°C}$ and $R_{H,\,50\,°C}$ both decrease. At higher molar ratios, $R_{H,\,20\,°C}$ increases again until reaching a molar ratio of 0.01 before the collapse of the microgels is triggered, whereas $R_{H,\,50\,°C}$ remains approximately constant (≈140–160 nm) with increasing molar ratio.

The morphology of the microgels for varying okanin concentrations during loading was investigated with STEM images (Fig. 3C). A rigidification of the microgels upon loading is observed, in line with the collapse of the microgels. Two distinct morphologies are observed for a molar ratio of 0.070. This might be indicative of an inhomogeneous loading within the microgels (core/shell) with different impacts on the particles' size. While the loading of the core leads to neglectable changes in particle size, the collapse of the dangling ends can cause a substantial size decrease. Therefore, at a molar ratio of 0.070, some microgels might already be nearly saturated whereas others are not, potentially leading to the wide structural variety for this okanin/CU ratio. This observation also explains the high standard deviation observed in DLS for a molar ratio of 0.070 (Fig. 3B). Surprisingly, the microgels shown in the STEM images already seem to be collapsed at a molar ratio of 0.070, which opposes the swelling determined by DLS (Fig. 3B). The drying of the microgels during the preparation of STEM samples can explain this difference. The removal of the solvent locally increases the okanin concentration and, thus, interactions between okanin and pVCL, that way enhancing the collapse.

To confirm the different effects on the size and morphology at low and high molar ratios observed by DLS, STEM and AFM images of the pVCL microgel with varying concentrations of okanin during the loading were recorded (Fig. S14). Height profiles (H_{AFM}) and the radius (R_{AFM}) of the microgels were obtained (Table 1). Due to the stiffness of the loaded microgels, the cantilever moved the particles during the AFM, making it impossible to determine the particles' width with this method. Instead, the width of saturated microgels was determined from STEM images (Fig. 3C). Histograms are shown in Fig. S15. Due to the rigid structure of the saturated microgels, the radius of the particle (R_{STEM}) can be determined, which is usually not accessible for diffuse microgels using STEM, as they spread on the surface.

Compared to the untreated microgel with H_{AFM} and R_{AFM} of 96 nm and 290 nm, respectively, okanin loading at a molar ratio of 0.002 leads to a decrease in H_{AFM} and R_{AFM} to 68 nm and 277 nm, respectively. This observation agrees with the decrease of $R_{H,\,20\,°C}$ at 0.002 and indicates the collapse of the microgel's shell. At the molar ratio of 0.070, H_{AFM} increases again to 138 nm, which is in line with the observed increase in

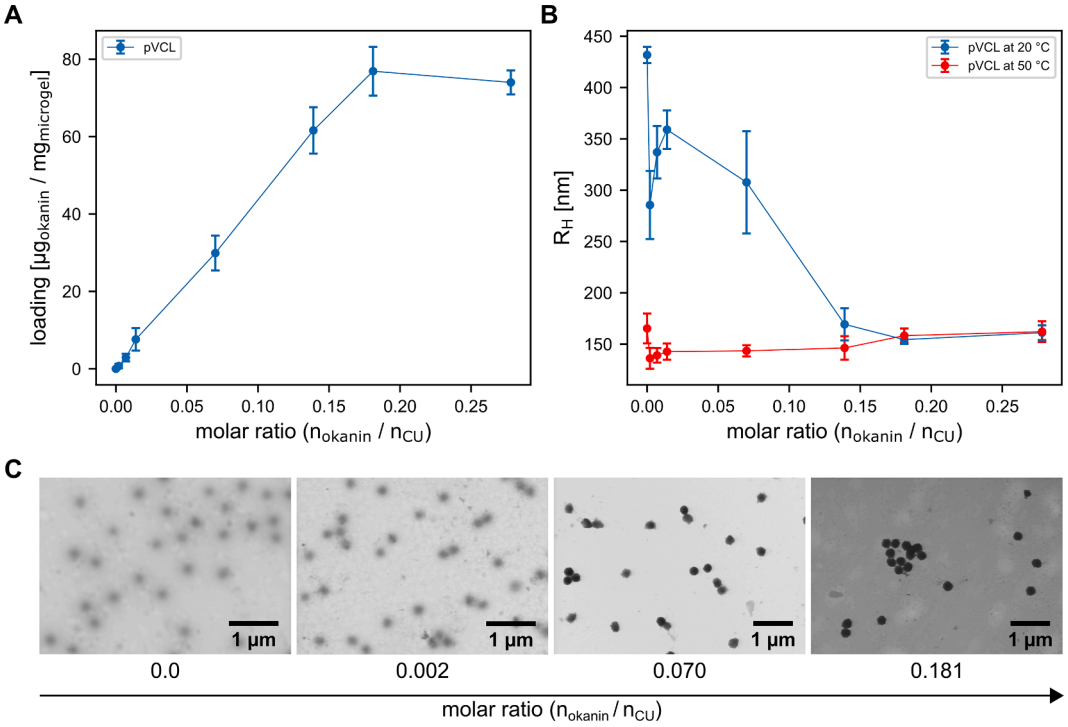

Fig. 3. Influence of the loading of okanin on the hydrodynamic radius, the thermo-responsiveness, and the morphology of pVCL microgels. A Loading of okanin into pure pVCL microgels determined by UV/Vis for varying molar ratios n_{okanin}/n_{CU}. B R_H of pVCL microgels before and after loading with okanin as determined by DLS at 20 °C and 50 °C for varying n_{okanin}/n_{CU} ratios. C Exemplary STEM images of a pVCL microgel for varying n_{okanin}/n_{CU} ratios.

Table 1
Okanin loadings and dimensions of the pVCL microgel for varying molar ratios of okanin/CU determined by DLS, AFM, and STEM.

Molar ratio (n_{okanin}/n_{CU})	Okanin loading [$\mu g_{okanin}/mg_{microgel}$]	$R_{H,\ 20\ °C}$ [nm]	$PDI_{20\ °C}$ [-]	$R_{H,\ 50\ °C}$ [nm]	$PDI_{50\ °C}$ [-]	R_{STEM} [nm]	R_{AFM} [nm]	H_{AFM} [nm]
0.000	0	432 ± 8	0.159 ± 0.023	165 ± 14	0.162 ± 0.014	n.a.[1]	290 ± 36	96 ± 10
0.002	0.7 ± 0.6	286 ± 33	0.111 ± 0.044	136 ± 10	0.081 ± 0.019	n.a.[1]	277 ± 34	68 ± 6
0.070	29.9 ± 4.5	308 ± 50	0.215 ± 0.172	144 ± 5	0.050 ± 0.031	115 ± 13	n.a.[2]	138 ± 17
0.181	76.9 ± 6.3	154 ± 4	0.041 ± 0.031	158 ± 7	0.036 ± 0.019	117 ± 7	n.a.[2]	257 ± 15

[1] Not available due to the diffuse morphology of the microgel.
[2] Not available due to the rigid, spherical morphology of the microgel.

$R_{H,\ 20\ °C}$. The deviation from $2 \times R_{STEM} = 230$ nm indicates that the microgels are still at least partly spread on the surface, in line with the previously described drying phenomenon. Finally, saturated microgels loaded at the high molar ratio of 0.181 show a height H_{AFM} of 257 ± 15 nm, which is in good agreement with $2 \times R_{STEM} = 234 \pm 14$ nm, supporting the formation of a rigid sphere. The height increase is caused by the collapse and rigidification as the morphology continuously transitions from a spreading structure to a sharply defined spherical one.

Observed changes in the microgel's size and morphology might be caused by the formation of non-covalent okanin-mediated intra-chain crosslinks. The deviation between loading at low and high molar ratios might be caused by the structural inhomogeneity of the microgel, i.e., the loosely crosslinked shell and the densely crosslinked core. While loading the core might lead to a slight decrease in the microgel's size, loading the shell and the accompanying collapse of the dangling chains might lead to the opposite effect. The strong decrease in size at very low molar ratios, however, might be explained by an increase in ionic strength, as it has been shown that ions and other osmolytes influence the phase transition of pVCL [78–79]. To validate our hypotheses and elucidate the interactions of okanin with the pVCL microgel at the atomistic scale, we performed molecular dynamics simulations.

3.2. Molecular dynamics simulations reveal a collapse of linear pVCL and compaction of crosslinked pVCL upon okanin loading

To elucidate the structural changes of the pVCL microgel upon okanin loading, we performed okanin loading simulations of linear and crosslinked pVCL representing the shell and the core of the microgel, respectively (Fig. 2). For linear pVCL and a molar ratio (n_{okanin}/n_{CU}) of 0.14, we observed a coil-to-globule transition triggered by okanin (Fig. S12, two and five out of ten trajectories for simulations at 293 K and 313 K, respectively). Interestingly, with higher amounts of okanin (molar ratio of 0.56 and 1.12), fewer coil-to-globule transitions are observed (Fig. S12). In general, the collapse of linear pVCL leads to a decrease in particle size (Fig. S12). For crosslinked pVCL, however, R_g and, thus, the size of the polymer increases slightly (Fig. S16 to Fig. S18) as the crosslinked pVCL forms porous structures (Fig. S19) with an increasing amount of okanin.

Visual inspection of the okanin binding to the pVCL models revealed that the binding can be categorized into two types (Fig. S20). The first type describes the frequent short-living adsorption of the okanin to only one polymer chain. The second type comprises molecules that are long-term bound to at least two chains, which may also be formed by a folded linear chain. To quantify the energetics of the two distinct binding types, we performed MM-PBSA calculations using trajectories of the linear pVCL, where a coil-to-globule transition occurred, as these trajectories comprise both types of interactions.

3.3. The collapse of linear pVCL and compaction of crosslinked pVCL is driven by minimizing the free energy of okanin binding

We performed MM-PBSA calculations on 490,000 frames from the simulation of a linear pVCL chain with a n_{okanin}/n_{CU} ratio of 0.14. We decided to use the results from the MM-PBSA analysis of okanin binding at a low n_{okanin}/n_{CU} ratio where stacking is not observed to focus on pure okanin microgel interactions. Considering MM-PBSA is an end-point method for estimating binding free energies, we only used frames where the okanin is at least adsorbed to the pVCL. The results of the MM-PBSA analysis for the adsorption and binding of okanin are depicted in Fig. 4.

The MM-PBSA analysis reveals an inverse correlation of $\Delta E_{MM} + \Delta G_{solvation}$ for an increasing number of contacts (Fig. 4A), i.e., the more contacts between the okanin and the pVCL, the more negative and, hence, favorable $\Delta E_{MM} + \Delta G_{solvation}$. Changes in the configurational entropy of the solutes (TΔS) upon the binding of okanin, however, are nearly independent of the number of formed contacts (Fig. 4B). Therefore, the resulting change in binding free energy, $\Delta G^0_{binding}$, shows an inverse correlation with the number of formed contacts, too. A linear correlation reveals that at ≈475 contacts, the unfavorable change in configurational entropy is outbalanced by the favorable change in $\Delta E_{MM} + \Delta G_{solvation}$. Note that for 38,824 frames where okanin has >475 contacts with the pVCL, the $\Delta G^0_{binding}$ values are normally distributed with a mean value of –2.68 kcal mol^{-1} (Fig. S13), indicating converged sampling of that property. The maximum number of contacts observed for the adsorption to a single pVCL chain is < 350 (Fig. S21 and Fig. S22). Thus, to achieve an energetically favorable binding pose, the okanin needs to be in contact with either at least two separate pVCL chains within a crosslinked pVCL microgel or within a collapsed linear chain. Within the crosslinked pVCL model, this promotes compaction as okanin forms interactions with two chains within the polymer network. For sections of the microgel containing dangling ends and a low crosslink density, comparable to the simulation using the linear pVCL oligomer, the binding of okanin leads to a substantial decrease in the particle size, as okanin promotes the coil-to-globule transition of single chains to achieve an energetically favorable binding mode.

The decomposition of ΔE_{MM} and $\Delta G_{solvation}$ yields further insights into the nature of interactions between the okanin and pVCL. ΔE_{MM} is decomposed into van der Waals (ΔE_{vdW}) and electrostatic energies (ΔE_{eel}) (eq (5)) as internal energies cancel due to the used one-trajectory approach. Upon okanin binding, both ΔE_{vdW} and ΔE_{eel} become increasingly favorable with an increasing number of formed contacts (Fig. S23). Although both terms show favorable energies for the binding of okanin, ΔE_{vdW} contributes ~ 2.5 times more (~–34.3 kcal mol^{-1} at 475 contacts, Fig. S23A) than ΔE_{eel} (~-13.3 kcal mol^{-1} at 475 contacts, Fig. S23B). As expected, both ΔE_{vdW} and ΔE_{eel} contribute more favorably to the binding of okanin with an increasing number of contacts between okanin and the oligomer.

Changes in $G_{solvation}$ upon binding can be decomposed into changes in polar G_{pol} and nonpolar G_{nonpol} contributions (eq (6)), where G_{nonpol} can be further decomposed into a repulsive cavitation solvation free energy term G_{cavity}, and an attractive dispersion solvation free energy term $G_{dispersion}$. With an increasing number of contacts, ΔG_{pol} decreases linearly, i.e., okanin binding becomes more favorable with an increasing number of contacts (Fig. S24A). The free energy needed for the endergonic processes of cavity formation (Fig. S24B) and dispersion (Fig. S24C), however, outweighs the aforementioned exergonic polar contribution, resulting in an overall unfavorable $\Delta G_{solvation}$.

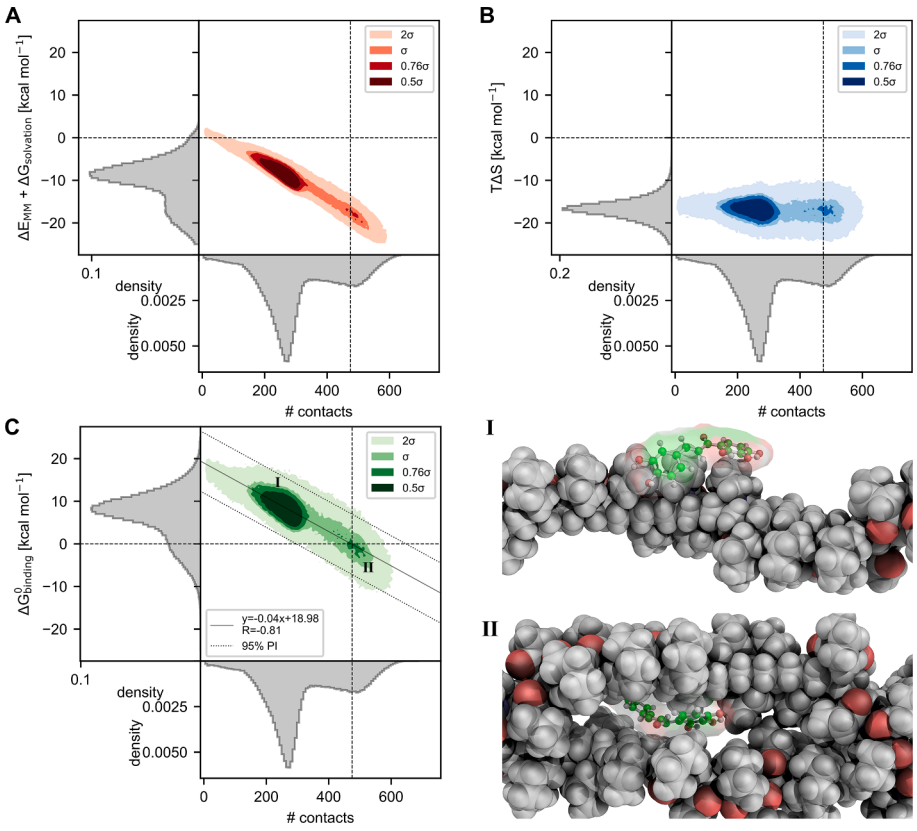

Fig. 4. Two-dimensional histograms of the binding free energy of okanin to the linear pVCL 50mer and its components (changes in the gas phase energy and solvation free energy ($\Delta E_{MM} + \Delta G_{solvation}$, A) and changes in the configurational entropy of the solutes ($T\Delta S$, B)) in relation to the number of formed contacts.. The binding free energy ($\Delta G^0_{binding}$, C) of okanin to the pVCL polymer shows an inverse linear correlation (regression line shown solid, 95 % prediction interval shown dotted, Pearson correlation coefficient and linear equation are depicted in the corresponding legend) with the number of formed contacts. Exemplary binding poses are shown for adsorbed okanin (I, < 475 contacts, $\Delta G^0_{binding} > 0$) and bound okanin (II, > 475 contacts, $\Delta G^0_{binding} < 0$). The MM-PBSA analysis was performed for trajectories of the linear pVCL 50mer, in which a collapse of the chain was observed; only frames where okanin formed contacts to pVCL were considered.

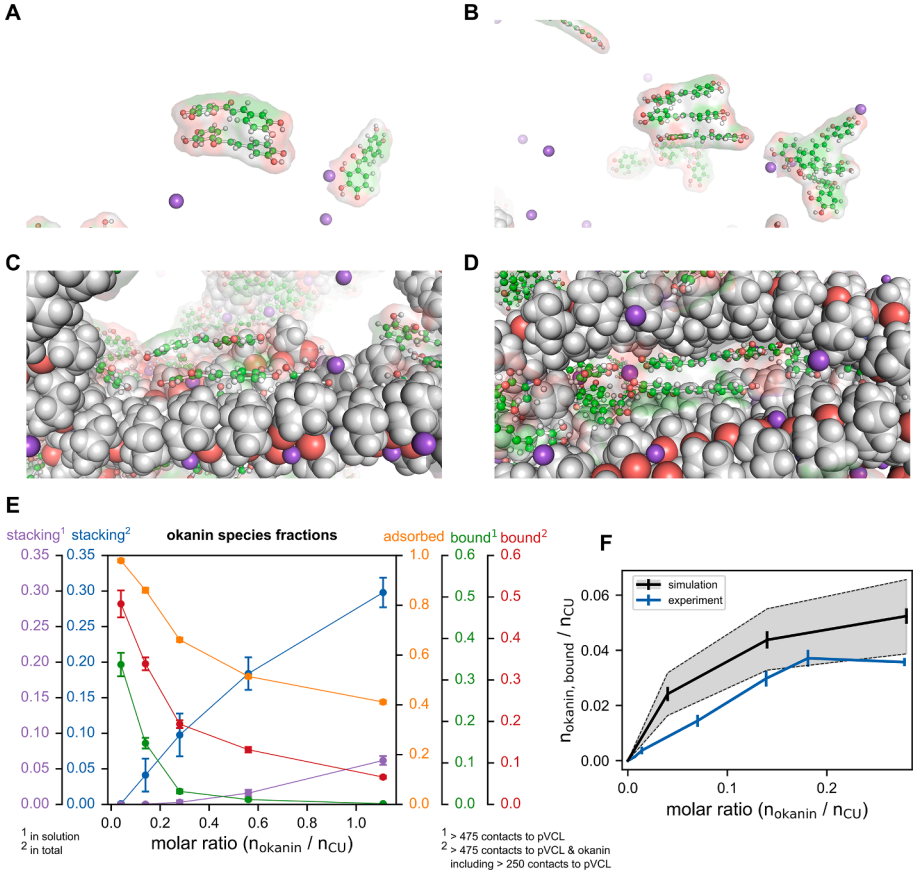

Fig. 5. Quantification of different okanin species and interactions. Okanin stacks in solution (A two molecules, B three molecules), on adsorbed okanin (C), and within a bound state (D) at a high molar ratio ($n_{okanin}/n_{CU} = 1.11$). E Quantification of okanin species. Okanin species fractions are given in relation to the overall number of okanin molecules within the respective system. With increasing okanin concentration, the fraction of okanin molecules in a stacking configuration in solution increases linearly for molar ratios above 0.28 (purple), while the overall fraction including stacking to bound/adsorbed okanin (blue) increases linearly for all molar ratios. The fraction of adsorbed (yellow), bound (green), and stacked within the microgel (red) okanin decreases with increasing okanin concentration. F Comparison of experimentally determined bound okanin per constitutional unit ($n_{okanin,bound}/n_{CU}$) with okanin considered bound and/or stacked within the microgel (>475 contacts to pVCL or > 475 contacts and at least 250 contacts formed with pVCL) in MD simulations. The grey shaded area depicts the uncertainty related to a change of the cutoff of ± 25 contacts (i.e., 450 and 500 contacts for the upper and lower bound, respectively), which corresponds to a change of the computed binding free energy of approximately ± 1 kcal mol^{-1}. (For interpretation of the references to colour in this figure legend, the reader is referred to the web version of this article.)

To evaluate whether the binding is mainly dominated by polar or nonpolar interactions, we calculated the sum of the electrostatic terms, i.e., ΔE_{eel} and ΔG_{pol}, and the nonpolar ones, i.e., ΔE_{vdW} and ΔG_{nonpol}. The former sum is favorable with -38.9 kcal mol^{-1} at 475 contacts, whereas the latter is unfavorable with 22.6 kcal mol^{-1} at 475 contacts due to ΔG_{nonpol}. Hence, according to the MM-PBSA analysis, polar interactions are the driving factor for okanin binding. Thus, we predict that the substitution or incorporation of moieties carrying additional (partially) charged moieties or hydrogen bond acceptors shall increase the okanin loading capacity of the microgel. This finding is well in line with using tannic acid as a supramolecular crosslinker for pVCL and other hydrogels, where hydrogen bonds were identified as the driving force for the physical crosslink [30,80].

3.4. MD simulations allow the quantification of different okanin species and interactions with respect to the okanin concentration in solution during loading

In our MD simulations, we identified increasing stacking interactions (Fig. 5A-D, Fig. S25) between the okanin molecules with increasing okanin concentrations. The stacking is observed for okanin in solution (Fig. 5A, B, Fig. S26) as well as for already adsorbed or bound okanin (Fig. 5C, D, Fig. S27 to Fig. S29). Thus, a second okanin molecule might be either stacked onto an adsorbed okanin molecule (Fig. 5C) or incorporated in the polymer-okanin-polymer configuration (Fig. 5D) previously identified as bound okanin based on free energy calculations (Fig. 4). The stacking of okanin inside the microgel might underlie the increased release of okanin from saturated microgels. The fraction of okanin found in a stacked configuration approximately linearly correlates with an increasing n_{okanin}/n_{CU} ratio (Fig. 5E (blue line)). In preliminary tests, we aimed at determining the amount of bound okanin as those with >475 contacts. However, with increasing n_{okanin}/n_{CU} ratio, this led to decreasing amounts of bound okanin (Fig. 5E (green line) and Fig. S27), although the number of adsorbed okanin molecules is less affected (Fig. 5E (yellow line) and Fig. S28). Including contacts to other okanin molecules (i.e., >475 contacts formed with the polymer and other okanin molecules with at least 250 contacts to the polymer) allows distinguishing bound and/or stacked okanin in the microgel (Fig. 5E (red line) and Fig. S29) from adsorbed okanin or okanin stacked in solution in simulations with higher okanin concentrations. Additionally to the contact-based identification and quantification of stacked okanin, we monitored the increase in stacking interactions between the okanin molecules using radial distribution functions ($g(r)$) of the distances between the aromatic rings. $g(r)$ substantially increases around 4 Å for molar ratios above 0.28 (Fig. S30), which supports the increased number of stacking interactions at high okanin concentrations.

In conclusion, for an increasing n_{okanin}/n_{CU} ratio, okanin-okanin interactions become increasingly important for the behavior in solution for molar ratios above 0.28, however, stacking on already adsorbed or bound okanin is preferred at all simulated molar ratios (Fig. S24–S28). In solution, the increase in okanin-okanin stacking potentially leads to experimentally observed precipitation of the dispersed okanin. For low okanin concentrations, we found that okanin is primarily bound between two polymer chains as this binding mode is energetically favorably. For high concentrations, however, we observe stacking of okanin onto already adsorbed okanin, replacing one polymer chain in the polymer-okanin-polymer structure. Furthermore, we observe the incorporation of an additional okanin molecule in the polymer-okanin-polymer structure.

Considering these cases, the amount of bound and/or stacked okanin within the microgel ($>$475 contacts to pVCL or >475 contacts to pVCL and at least 250 contacts formed with the polymer) observed in simulations with increasing okanin concentration semi-quantitatively matches the experimentally determined loadings, particularly for n_{okanin}/n_{CU} ratios >0.14 (Fig. 5F). The slight overestimation of bound okanin in the simulations might be due to different length scales of the microgel particles with respect to the experiment, which may impact the access of okanin to the microgel or the egress in comparison to experimental loading/washing. Another reason might be the loss of okanin during the washing steps performed in the experimental loading process (Fig. 1).

3.5. Incorporating GMA into pVCL microgels increases the overall loading capacity without changing the saturation concentration

To improve the loading capacity of pVCL-based microgels, we investigated the nature of the interactions between okanin and the pVCL microgel by MM-PBSA calculations. The calculations revealed that polar interactions are the driving factors for okanin binding to the microgel. Thus, we predicted that incorporating moieties carrying additional (partially) charged moieties or an increased number of hydrogen bond acceptors might benefit okanin loading.

To validate our hypothesis, we investigated the influence of GMA incorporation (10 mol%) on the loading capacity, as it contains more potential hydrogen bond acceptors [32]. To determine the influence of the localization of GMA, GMA was incorporated into the shell (p(VCL/GMA_{shell})) and the core (p(VCL/GMA_{core})). The amount of okanin-loaded into the p(VCL-*co*-GMA) microgels was determined analogously to pVCL using UV/Vis spectroscopy. The spectra are shown in Fig. S31 and Fig. S32 and the results are depicted in Fig. 6A.

The loading increases linearly for both p(VCL-*co*-GMA) microgels analogous to the pure pVCL microgel. Saturation of the microgels is achieved at a molar ratio of 0.18, independent of the microgel variant. The loading capacity of both p(VCL-*co*-GMA) microgels is ≈ 150 µg/mg and, thus, twofold as large as the loading capacity of the pure pVCL microgel (≈ 75 µg/mg). A high amount of precipitate during the loading of okanin into p(VCL-*co*-GMA) at the highest okanin concentration led to larger errors in the amount of loaded okanin. For this reason, loading at even higher okanin concentrations is not accessible through experiment.

Surprisingly, the localization of the GMA within the microgel does not influence the loading of okanin as the loading profiles of p(VCL/GMA_{shell}) and p(VCL/GMA_{core}) are virtually identical (Fig. 6A). We hypothesize that localization of the GMA-rich polymer segments in the microgel shell will enhance their accessibility and make okanin loading more efficient. $R_{H,\ 20\,°C}$ and $R_{H,\ 50\,°C}$ were determined for both p(VCL-*co*-GMA) microgels by DLS (Table S13). To determine if the collapse/compaction depends on the amount of bound okanin independent of the composition, $R_{H,\ 20\,°C}$ for all three microgel variants is plotted as a function of the loading and normalized to the size of the unloaded microgel, yielding the normalized hydrodynamic radius $R_{H,\ normed}$ (Table S13). The overall trend of $R_{H,\ normed}$ is similar for all three microgel variants (Fig. 6B). The collapse of the GMA-containing microgels was also confirmed by AFM images (Fig. S33 and Fig. S34) and STEM images (Fig. S35 to Fig. S37). Analogous to the loading profile, the localization of the GMA within the microgels does not influence the changes in the microgel's size. Interestingly, the collapse of the microgel is triggered at loadings of 60–75 µg/mg, independent of the microgel composition. This is indicative of a critical amount of okanin necessary to mediate non-covalent inter-chain crosslinks to trigger the collapse of the microgels. Moreover, further loading of okanin is observed even after the full collapse of the microgels. Thus, okanin molecules might bind onto the surface of the microgel at this point, or the collapse of the microgel might generate other sites within the microgel that are favorable for the binding of okanin.

3.6. Experiments and simulations show that the co-solvent-triggered release of okanin is more efficient than the release in pure water

For a controlled release of okanin, a suitable trigger is required to manipulate the interactions between okanin and its carrier. Green solvents depict promising candidates to shift the equilibrium between bound and unbound okanin by influencing the intermolecular

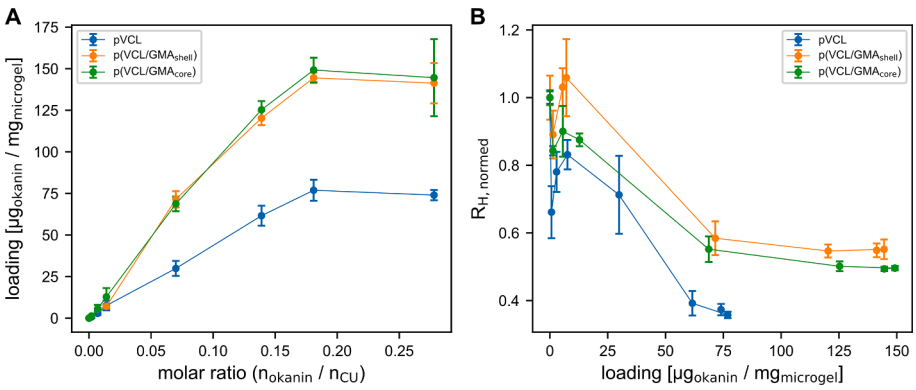

Fig. 6. Determined okanin loading capacity of pVCL and p(VCL-*co*-GMA) microgels and effect on the microgel size. A Loading of okanin into pVCL and p(VCL-*co*-GMA) microgels determined by UV/Vis in dependency of the molar ratio n_{okanin}/n_{CU}. B $R_{H,\ normed}$ of pVCL and p(VCL-*co*-GMA) microgels determined by DLS at 20 °C.

interactions within the system. As release agents, we chose the green solvents EtOAc, DMSO, and AcOH. DMSO and AcOH are commonly used in agricultural formulations. The EtOAc was chosen as an organic solvent reference and as a benchmark. The co-solvent triggered release from pure pVCL microgels loaded at n_{okanin}/n_{CU} ratios of 0.07 and 0.18 were investigated by adding 9.4 vol-% of EtOAc to the microgel dispersion. A reference was obtained by adding the same volume of water. The release of okanin in relation to the initial loading was determined via UV/Vis spectroscopy. Simultaneously, we investigated the co-solvent-induced release of okanin in MD simulations (see Quantification of okanin released during release simulations in water and water/ethyl acetate in the Materials and Methods). The comparison of both results is depicted in Fig. 7A.

The relative release of pVCL loaded at a lower okanin is also lower than the release from microgels loaded at higher okanin concentration (Fig. S38 to Fig. S41 for simulation / Fig. S42 and Fig. S43 for experiments). For a low okanin loading, the release of okanin in water (2.7 %) and EtOAc (10.7 %) observed in experiments matches the observed release in MD simulations. For the pVCL microgel loaded at a high okanin concentration, 7.0 % of the bound okanin molecules are released in water, whereas the release increases to 15.9 % for EtOAc. The release observed in MD simulations also matches the experimental results for water and slightly overestimates the release in EtOAc. For the release in water, however, the overall number of released okanin molecules is

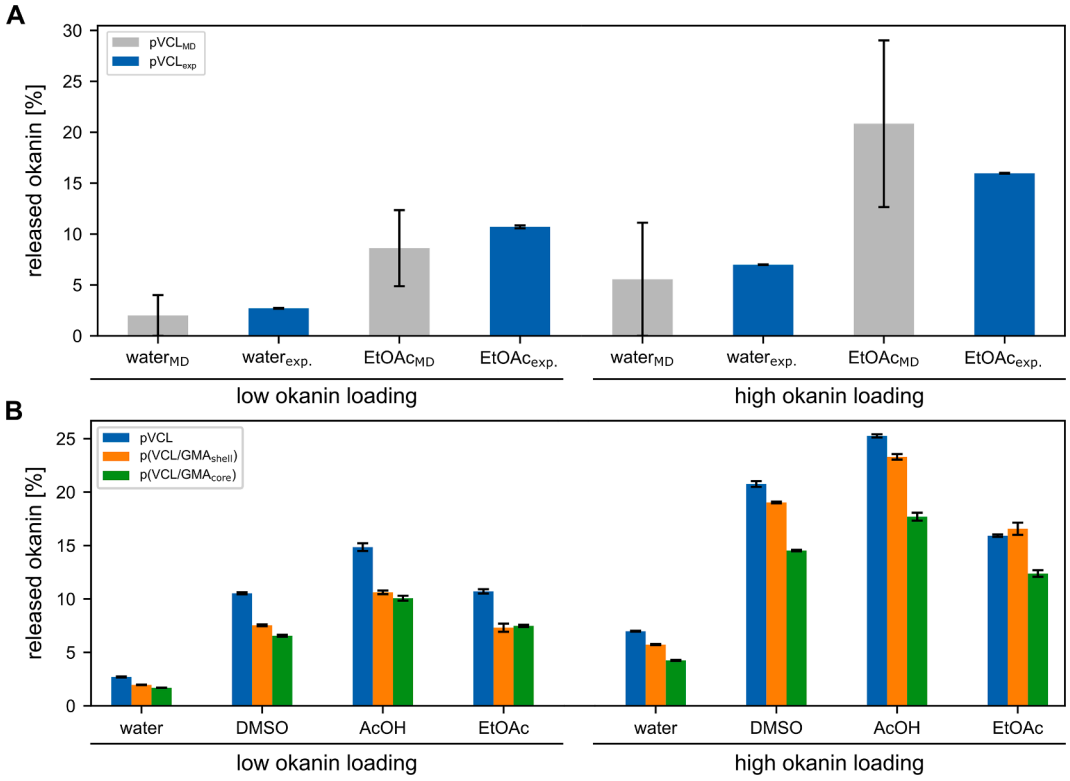

Fig. 7. Co-solvent-triggered release of okanin in experiments and simulations. A Comparison of experimentally observed okanin release for EtOAc with release observed in MD simulations. The experimental values are compared to the release in MD simulations observed for microgels loaded at low okanin loadings ($n_{okanin}/n_{CU} = 0.04$ and $n_{okanin}/n_{CU} = 0.07$ for MD and experiment, respectively) and high okanin loading ($n_{okanin}/n_{CU} = 0.28$ and $n_{okanin}/n_{CU} = 0.18$ for MD and experiment, respectively). B Experimentally observed okanin release for different co-solvents (DMSO, AcOH, and EtOAc) for low ($n_{okanin}/n_{CU} = 0.07$) and high ($n_{okanin}/n_{CU} = 0.18$) okanin concentrations at loading. The initial loadings were 31.1 µg/mg and 73.0 µg/mg for pVCL, 65.7 µg/mg and 146.0 µg/mg for p(VCL/GMA$_{core}$) and 72.3 µg/mg and 144.2 µg/mg for p(VCL/GMA$_{shell}$).

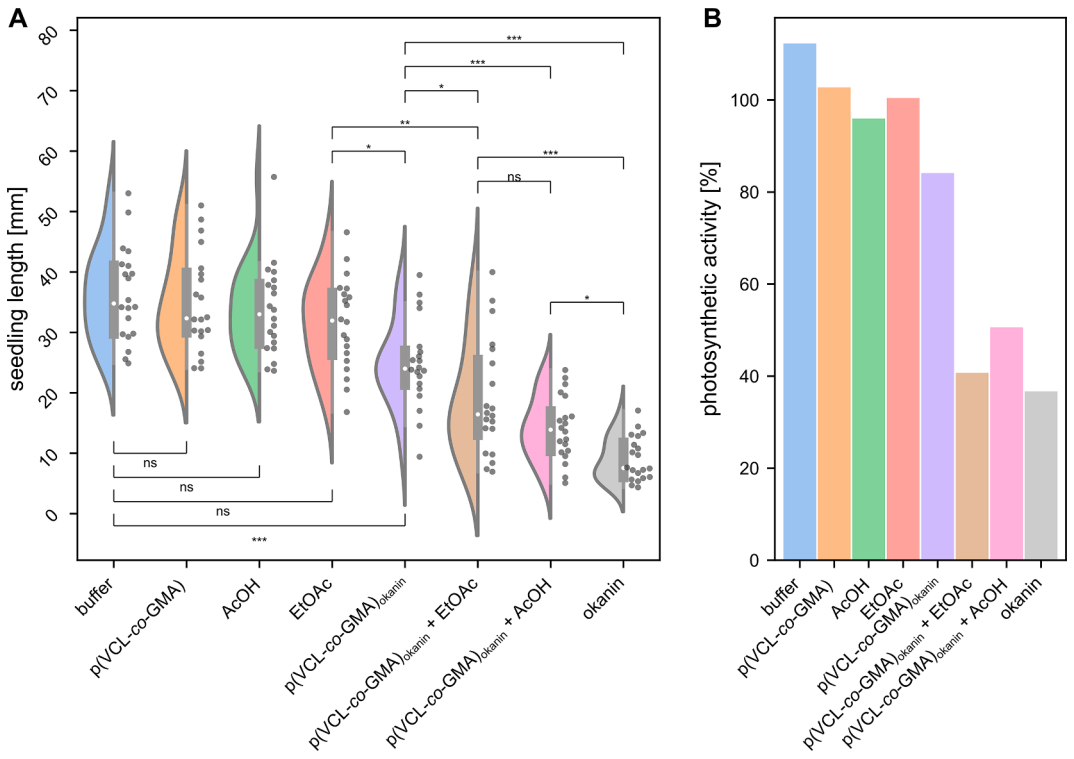

Fig. 8. A Impact of organic solvents used for a triggered release, loaded and unloaded microgels, and combinations thereof on *A. retroflexus* seedling growth. Significance is evaluated using a two-sided Mann-Whitney *U* test; corresponding *p*-values are provided above/below the horizontal lines (ns: "not significant", *: $p \leq 0.05$, ***: $p \leq 0.001$; $n = 20$). The white dot displays the mean, the bars depict the quartiles. B Impact of organic solvents used for a triggered release, loaded and unloaded microgels, and combinations thereof on the relative photosynthetic activity of adult *A. retroflexus* plants. Photosynthetic activity before treatment was taken for reference (100 %) ($n = 1$).

lower and the desorption event is less likely. Thus, further sampling or increasing the system size might be necessary to further decrease the uncertainty in the estimated amount of released okanin.

Besides EtOAc, we investigated the effect of other common green solvents. We chose DMSO due to the high solubility of okanin and AcOH to probe the influence of a protic solvent. The results for the release from pVCL as well as p(VCL/GMA_{shell}) and p(VCL/GMA_{core}) are depicted in Fig. 7B. Both solvents further increase the release compared to EtOAc, with the highest release observed for AcOH (25.3 %). The observed trends for the different solvents are similar for all microgel variants, irrespective of the okanin concentration during loading. Although the relative release of okanin is decreased for the p(VCL-*co*-GMA) microgels, the absolute amount of okanin released is higher due to higher loading (Fig. S43). The decreased relative release for the p(VCL-*co*-GMA) microgels compared to the pure pVCL microgel may be due to the okanin forming stronger interactions with the GMA moieties. Interestingly, the incorporation of GMA in the core decreases the release stronger than in the shell, regardless of the amount of loaded okanin. This effect, however, is more pronounced for saturated microgels. Thus, we assume that the okanin is preferentially localized within the GMA-rich sections of the microgel. In the case of p(VCL/GMA_{shell}), the okanin is mainly bound to the shell from which a release is easier, whereas the release is hindered by diffusive traps in p(VCL/GMA_{core}), especially for (partially) collapsed microgels.

3.7. Seedling assays and measurements of relative photosynthetic activity yield proof–of–principle for the application on A. retroflexus plants

Seedlings of the C_4-weed *A. retroflexus* were germinated on paper and treated with p(VCL-*co*-GMA) microgels saturated with okanin, p(VCL/GMA_{shell}) microgels saturated with okanin and EtOAc as a solvent-release trigger, p(VCL/GMA_{shell}) microgels saturated with okanin and AcOH as a solvent-release trigger, and a buffer solution saturated with okanin plus the respective controls (Fig. 8A). Treatments with the unloaded p(VCL/GMA_{shell}) microgels, AcOH, and EtOAc either result in insignificant differences or, for EtOAc, negligible differences compared to the control treated with buffer. All okanin-containing treatments result in significantly shorter seedlings than the controls. Solvent-triggered release of okanin yields significantly shorter seedlings than the ones treated solely with p(VCL/GMA_{shell}) microgels saturated with okanin; EtOAc or AcOH as release triggers do not lead to significantly different results. Buffer saturated with okanin results in the shortest seedling lengths. Note, however, that we did not test the influence of a potential wash-off, where microgels saturated with okanin might have an advantage over buffer saturated with okanin.

Likewise, on adult *A. retroflexus* plants, relative photosynthetic activity was determined for the above treatments (Fig. 8B). The controls show minor differences to the activity before treatment (~100 %). Okanin released from p(VCL/GMA_{shell}) microgels yields an activity of ~ 80 %. By contrast, solvent-triggered release of okanin from p(VCL/GMA_{shell}) microgels results in a similar activity as okanin-saturated buffer, i.e., ~40 – 50 % of remaining photosynthetic activity.

3.8. Putative scope of the approach

To evaluate if the pVCL-based microgels might be suitable for other established agrochemicals, we compared the shape and chemical features of okanin to 2634 known herbicides, fungicides, insecticides, or pesticides (see Supplemental Materials and Methods, Fig. S44). The comparison of shape peaks around 0.75 (on a scale from 0 to 1 with 1 indicating perfect agreement), and the joint shape and chemical features comparison at 0.90 (on a scale from 0 to 2 with 2 indicating perfect agreement), indicating that, on average, the molecules are about halfway similar to okanin. We found several commercial herbicides, like

Bromfenoxim, Aclonifen, Thifensulfuron-methyl, and Metsulfuron-methyl (Fig. S45) that are similar to okanin, suggesting that pVCL-based microgels might also be a suitable carrier for them.

4. Conclusion

In this study, we investigated pVCL-based microgels as a potential carrier for okanin, an inhibitor of a C_4 plant key enzyme, in an integrated approach using experiments and simulations. The presented pVCL-based carriers should allow for tailoring the loading of okanin molecules, stabilization of okanin molecules in aqueous solution, and smart on-demand delivery of its cargo by exploiting release triggers such as treatment with aqueous co-solvents. DLS, AFM, and TEM analysis revealed that upon loading of okanin, pVCL microgels collapse and rigidify. The loading profile, i.e., the amount of loaded okanin with respect to the okanin concentration during loading, was determined using UV/Vis spectroscopy. By performing molecular dynamics simulations of oligomeric and crosslinked pVCL in combination with free energy calculations, we identified two different binding modes of okanin. Besides the adsorption of okanin to the pVCL chains, we found energetically favorable binding modes in which okanin mediates interchain crosslinks. For high okanin concentrations, we furthermore find stacking interactions of okanin not only within the solution but also with already adsorbed or bound okanin. Considering these states, the amount of bound okanin observed in simulations is in line with the experimentally determined loading profile. These findings can explain the experimentally observed collapse of the microgels and the rigidification of the particles. Decomposition of the binding free energy revealed polar interactions as a driving factor for okanin binding. Based on these results, we synthesized two p(VCL-*co*-GMA) microgels, where the GMA is localized within either the shell or core sections of the microgel. Independent of the GMA localization, the overall loading capacity of the microgels for okanin is doubled. Finally, we investigated the triggered release of okanin from the microgels by the addition of green solvents. Application of okanin-loaded p(VCL/GMA_{shell}) microgels to seedlings and adult plants of *A. retroflexus* confirm the *in vitro* experiments and demonstrate a proof-of-principle for the application on plants.

Our findings show that p(VCL-*co*-GMA) microgels are promising potential carriers for the herbicide okanin. Next to the increased loading capacity of pVCL microgels that incorporate GMA, epoxy groups can be used for an easy surface modification of the microgel. If the epoxy groups are located within the shell of the microgel, they can be used to attach anchor peptides [37] to achieve an increased rain fastness of the carrier on the plant leaves. Finally, green solvents effectively triggered the (partial) release okanin, which provides a targeted way to release okanin on-demand. For the field application, this can potentially be achieved by a second spraying with an aqueous solution of a green solvent. Hence, this work establishes a basis for the further optimization of pVCL-based microgels for the delivery of herbicides with chemical properties such as okanin. In future works, the formulation efficiency in plant application has to be tested.

Author contributions

J.D.[†] generated the atomistic models, performed the computational studies, analyzed results, and wrote the manuscript; F.K.[†] designed experiments, performed experimental studies, analyzed results, and wrote the manuscript; A.T. conceptualized experiments, analyzed results, and wrote the manuscript; A.H. designed, performed analyzed plant studies; G.G. contributed to conceiving the project, supervised and managed plant studies. A.P. conceived the study, supervised and managed the project, and wrote the manuscript; H.G. conceived the study, supervised and managed the project, and wrote the manuscript. All authors have approved the final version of the manuscript. [†]These authors contributed equally.

Funding sources

This research is part of the scientific activities of the Bioeconomy Science Center, which were financially supported by the Ministry of Innovation, Science and Research of the German Federal State of North Rhine-Westphalia (MIWF) within the framework of the NRW Strategy Project BioSC (No. 313/323-400-00213) (funds to HG, AP, and GG within the FocusLab greenRelease). This work was performed in collaboration with the Center for Chemical Polymer Technology (CPT), which was supported by the EU (EUSMI, 731019) and the federal state of North Rhine-Westphalia (grant EFRE 300088302). We greatly acknowledge the Deutsche Forschungsgemeinschaft for financial support within the Collaborative Research Center SFB 985 “Functional Microgels and Microgel Systems”.

Declaration of Competing Interest

The authors declare that they have no known competing financial interests or personal relationships that could have appeared to influence the work reported in this paper.

Data availability

Data will be made available on request. The library (lib) and parameter modification (frcmod) files used in this study are available at http://dx.doi.org/10.25838/d5p-41.

Acknowledgements

We gratefully acknowledge the computational support provided by the “Center for Information and Media Technology” (ZIM) at the Heinrich Heine University Düsseldorf and the computing time provided by the John von Neumann Institute for Computing (NIC) on the supercomputer JUWELS at Jülich Supercomputing Centre (JSC) (user IDs: HKF7, microgels). We are grateful to OpenEye for an academic license. We greatly acknowledge Hannah Mathews and Nadja Wolter, who performed STEM measurements as well as Marta Santi, who prepared samples for AFM and conducted the AFM measurements.

Appendix A. Supplementary data

Supplementary data to this article can be found online at https://doi.org/10.1016/j.cej.2023.141631.

References

[1] J. Popp, K. Pető, J. Nagy, Pesticide productivity and food security A review, Agronomy for Sustainable Development 33 (1) (2013) 243–255.
[2] M. Hunsche, A. Alexeenko, L. Damerow, G. Noga, Rain-induced removal of copper from apple leaves: Influence of rain properties and tank-mix adjuvants on deposit characteristics at the micro scale, Crop Prot. 30 (4) (2011) 495–501.
[3] X. Zhao, H. Cui, Y. Wang, C. Sun, B. Cui, Z. Zeng, Development Strategies and Prospects of Nano-based Smart Pesticide Formulation, J. Agric. Food Chem. 66 (26) (2018) 6504–6512.
[4] A. Roy, S. Singh, J. Bajpai, A. Bajpai, Controlled pesticide release from biodegradable polymers, Open Chem. 12 (4) (2014) 453–469.
[5] C.G. Athanassiou, N.G. Kavallieratos, G. Benelli, D. Losic, P. Usha Rani, N. Desneux, Nanoparticles for pest control: current status and future perspectives, J. Pest. Sci. 91 (1) (2018) 1–15.
[6] S. Savary, L. Willocquet, S.J. Pethybridge, P. Esker, N. McRoberts, A. Nelson, The global burden of pathogens and pests on major food crops, Nat. Ecol. Evol. 3 (3) (2019) 430–439.
[7] E.C. Oerke, Crop losses to pests, J. Agric. Sci. 144 (1) (2006) 31–43.
[8] G.T.T. Nguyen, G. Erlenkamp, O. Jäck, A. Küberl, M. Bott, F. Fiorani, H. Gohlke, G. Groth, Chalcone-based Selective Inhibitors of a C4 Plant Key Enzyme as Novel Potential Herbicides, Sci. Rep. 6 (1) (2016) 27333.
[9] N. Chotsaeng, C. Laosinwattana, P. Charoenying, Herbicidal Activity of Flavokawains and Related trans-Chalcones against Amaranthus tricolor L. and Echinochloa crus-galli (L.) Beauv, ACS Omega 4 (24) (2019) 20748–20755.
[10] X. Liu, Y. Chen, Y. Deng, C. Xiao, S. Luan, Q. Huang, Novel Galactosyl Moiety-Conjugated Furylchalcones Synthesized Facilely Display Significant Regulatory Effect on Plant Growth, J. Agric. Food Chem. 70 (6) (2022) 1766–1775.

[11] A. Minges, D. Janßen, S. Offermann, G. Groth, Efficient In Vivo Screening Method for the Identification of C4 Photosynthesis Inhibitors Based on Cell Suspensions of the Single-Cell C4 Plant Bienertia sinuspersici, Frontiers Plant Sci. (2019) 10.

[12] F.A. Plamper, W. Richtering, Functional Microgels and Microgel Systems, Acc. Chem. Res. 50 (2) (2017) 131–140.

[13] M. Karg, A. Pich, T. Hellweg, T. Hoare, L.A. Lyon, J.J. Crassous, D. Suzuki, R. A. Gumerov, S. Schneider, I.I. Potemkin, W. Richtering, Nanogels and Microgels: From Model Colloids to Applications, Recent Developments, and Future Trends, Langmuir 35 (19) (2019) 6231–6255.

[14] M. Dirksen, C. Dargel, L. Meier, T. Brändel, T. Hellweg, Smart microgels as drug delivery vehicles for the natural drug aescin: uptake, release and interactions, Colloid Polym. Sci. 298 (6) (2020) 505–518.

[15] H. Vihola, A. Laukkanen, J. Hirvonen, H. Tenhu, Binding and release of drugs into and from thermosensitive poly(N-vinyl caprolactam) nanoparticles, Eur. J. Pharm. Sci. 16 (1) (2002) 69–74.

[16] T. Hoare, R. Pelton, Impact of Microgel Morphology on Functionalized Microgel−Drug Interactions, Langmuir 24 (3) (2008) 1005–1012.

[17] R.A. Meurer, S. Kemper, S. Knopp, T. Eichert, F. Jakob, H.E. Goldbach, U. Schwaneberg, A. Pich, Biofunctional Microgel-Based Fertilizers for Controlled Foliar Delivery of Nutrients to Plants, Angew. Chem. Int. Ed. 56 (26) (2017) 7380–7386.

[18] Y. Wang, J. Nie, B. Chang, Y. Sun, W. Yang, Poly(vinylcaprolactam)-Based Biodegradable Multiresponsive Microgels for Drug Delivery, Biomacromolecules 14 (9) (2013) 3034–3046.

[19] X. Li, H. Li, C. Zhang, A. Pich, L. Xing, X. Shi, Intelligent nanogels with self-adaptive responsiveness for improved tumor drug delivery and augmented chemotherapy, Bioact. Mater. 6 (10) (2021) 3473–3484.

[20] X. Li, H. Sun, H. Li, C. Hu, Y. Luo, X. Shi, A. Pich, Multi-Responsive Biodegradable Cationic Nanogels for Highly Efficient Treatment of Tumors, Adv. Funct. Mater. 31 (26) (2021) 2100227.

[21] T. Belthle, D.E. Demco, A. Pich, Nanostructuring the Interior of Stimuli-Responsive Microgels by N-Vinylimidazoles Quaternized with Hydrophobic Alkyl Chains, Macromolecules 55 (3) (2022) 844–861.

[22] W.H. Blackburn, E.B. Dickerson, M.H. Smith, J.F. McDonald, L.A. Lyon, Peptide-Functionalized Nanogels for Targeted siRNA Delivery, Bioconjug. Chem. 20 (5) (2009) 960–968.

[23] M. Malmsten, H. Bysell, P. Hansson, Biomacromolecules in microgels — Opportunities and challenges for drug delivery, Curr. Opin. Colloid Interface Sci. 15 (6) (2010) 435–444.

[24] F. Li, C. Wang, W. Guo, Multifunctional Poly-N-Isopropylacrylamide/DNAzyme Microgels as Highly Efficient and Recyclable Catalysts for Biosensing, Adv. Funct. Mater. 28 (10) (2018) 1705876.

[25] D. Steinhilber, T. Rossow, S. Wedepohl, F. Paulus, S. Seiffert, R. Haag, A Microgel Construction Kit for Bioorthogonal Encapsulation and pH-Controlled Release of Living Cells, Angew. Chem. Int. Ed. 52 (51) (2013) 13538–13543.

[26] H. Vihola, A. Laukkanen, L. Valtola, H. Tenhu, J. Hirvonen, Cytotoxicity of thermosensitive polymers poly(N-isopropylacrylamide), poly(N-vinylcaprolactam) and amphiphilically modified poly(N-vinylcaprolactam), Biomaterials 26 (16) (2005) 3055–3064.

[27] Y. Du, E. Lo, S. Ali, A. Khademhosseini, Directed assembly of cell-laden microgels for fabrication of 3D tissue constructs, Proc. Natl. Acad. Sci. U.S.A. 105 (28) (2008) 9522–9527.

[28] J. Ramos, A. Imaz, J. Forcada, Temperature-sensitive nanogels: poly(N-vinylcaprolactam) versus poly(N-isopropylacrylamide), Polym. Chem. 3 (4) (2012) 852–856.

[29] R. Schroeder, W. Richtering, I.I. Potemkin, A. Pich, Stimuli-Responsive Zwitterionic Microgels with Covalent and Ionic Cross-Links, Macromolecules 51 (17) (2018) 6707–6716.

[30] C.M. López, A. Pich, Supramolecular Stimuli-Responsive Microgels Crosslinked by Tannic Acid, Macromol. Rapid Commun. 39 (6) (2018) 1700808.

[31] S.H. Jung, S. Bulut, L.P.B. Busca Guerzoni, D. Günther, S. Braun, L. De Laporte, A. Pich, Fabrication of pH-degradable supramacromolecular microgels with tunable size and shape via droplet-based microfluidics, J. Colloid Interface Sci. 617 (2022) 409–421.

[32] N. Häntzschel, F. Zhang, F. Eckert, A. Pich, M.A. Winnik, Poly(N-vinylcaprolactam-co-glycidyl methacrylate) Aqueous Microgels Labeled with Fluorescent LaF3: Eu Nanoparticles, Langmuir 23 (21) (2007) 10793–10800.

[33] N. Häntzschel, R.-D. Hund, H. Hund, M. Schrinner, C. Lück, A. Pich, Hybrid Microgels with Antibacterial Properties, Macromol. Biosci. 9 (5) (2009) 444–449.

[34] E. Gau, D.M. Mate, Z. Zou, A. Oppermann, A. Töpel, F. Jakob, D. Wöll, U. Schwaneberg, A. Pich, Sortase-Mediated Surface Functionalization of Stimuli-Responsive Microgels, Biomacromolecules 18 (9) (2017) 2789–2798.

[35] A. Singh, N. Dhiman, A.K. Kar, D. Singh, M.P. Purohit, D. Ghosh, S. Patnaik, Advances in controlled release pesticide formulations: Prospects to safer integrated pest management and sustainable agriculture, J. Hazard. Mater. 385 (2020), 121525.

[36] M.E. Trenkel, Slow- and Controlled-release and Stabilized Fertilizers,An Option for Enhancing Nutrient Use Efficiency in Agriculture, International Fertilizer Industry Association (2010).

[37] J. Dittrich, C. Brethauer, L. Goncharenko, J. Bührmann, V. Zeisler-Diehl, S. Pariyar, F. Jakob, T. Kurkina, L. Schreiber, U. Schwaneberg, H. Gohlke, Rational Design Yields Molecular Insights on Leaf-Binding of Anchor Peptides, ACS Appl. Mater. Interfaces (2022).

[38] M.A. Shahid, A. Sarkhosh, N. Khan, R.M. Balal, S. Ali, L. Rossi, C. Gómez, N. Mattson, W. Nasim, F. Garcia-Sanchez, Insights into the Physiological and Biochemical Impacts of Salt Stress on Plant Growth and Development, Agronomy 10 (7) (2020) 938.

[39] T.J. Flowers, A. Garcia, M. Koyama, A.R. Yeo, Breeding for salt tolerance in crop plants — the role of molecular biology, Acta Physiol. Plant. 19 (4) (1997) 427–433.

[40] D. Prat, A. Wells, J. Hayler, H. Sneddon, C.R. McElroy, S. Abou-Shehada, P.J. Dunn, CHEM21 selection guide of classical- and less classical-solvents, Green Chem. 18 (1) (2016) 288–296.

[41] K. Alfonsi, J. Colberg, P.J. Dunn, T. Fevig, S. Jennings, T.A. Johnson, H.P. Kleine, C. Knight, M.A. Nagy, D.A. Perry, M. Stefaniak, Green chemistry tools to influence a medicinal chemistry and research chemistry based organisation, Green Chem. 10 (1) (2008) 31–36.

[42] D. Nečas, P. Klapetek, Gwyddion: an open-source software for SPM data analysis, Open Physics 10 (1) (2012) 181–188.

[43] W. Rasband, ImageJ,, Image processing and analysis in Java. *Astrophysics Source Code*, Library ascl (2012) 1206.013.

[44] A. Balaceanu, Y. Verkh, D. Kehren, W. Tillmann, A. Pich, Thermoresponsive Core-Shell Microgels Synthesis and Characterisation, *Z. Phys. Chem.* 228 (2–3) (2014) 253–267.

[45] W.L. Jorgensen, J. Chandrasekhar, J.D. Madura, R.W. Impey, M.L. Klein, Comparison of simple potential functions for simulating liquid water, J. Chem. Phys. 79 (2) (1983) 926–935.

[46] J. Dittrich, M. Kather, A. Holzberger, A. Pich, H. Gohlke, Cumulative Submillisecond All-Atom Simulations of the Temperature-Induced Coil-to-Globule Transition of Poly(N-vinylcaprolactam) in Aqueous Solution, Macromolecules 53 (22) (2020) 9793–9810.

[47] S. Izadi, R. Anandakrishnan, A.V. Onufriev, Building Water Models: A Different Approach, J. Phys. Chem. Lett. 5 (21) (2014) 3863–3871.

[48] C.I. Bayly, P. Cieplak, W. Cornell, P.A. Kollman, A well-behaved electrostatic potential based method using charge restraints for deriving atomic charges: the RESP model, J. Phys. Chem. 97 (40) (1993) 10269–10280.

[49] M.J. Frisch G.W. Trucks H.B. Schlegel G.E. Scuseria M.A. Robb J.R. Cheeseman G. Scalmani V. Barone B. Mennucci G.A. Petersson H. Nakatsuji M. Caricato X. Li H.P. Hratchian A.F. Izmaylov J. Bloino G. Zheng J.L. Sonnenberg M. Hada M. Ehara K. Toyota R. Fukuda J. Hasegawa M. Ishida T. Nakajima Y. Honda O. Kitao H. Nakai T. Vreven J.A. Montgomery Jr., Peralta, J. E., Ogliaro, F., Bearpark, M., Heyd, J. J., Brothers, E., Kudin, K. N., Staroverov, V. N., Kobayashi, R., Normand, J., Raghavachari, K., Rendell, A., Burant, J. C., Iyengar, S. S., Tomasi, J., Cossi, M., Rega, N., Millam, J. M., Klene, M., Knox, J. E., Cross, J. B., Bakken, V., Adamo, C., Jaramillo, J., Gomperts, R., Stratmann, R. E., Yazyev, O., Austin, A. J., Cammi, R., Pomelli, C., Ochterski, J. W., Martin, R. L., Morokuma, K., Zakrzewski, V. G., Voth, G. A., Salvador, P., Dannenberg, J. J., Dapprich, S., Daniels, A. D., Farkas, Ö., Foresman, J. B., Ortiz, J. V., Cioslowski, J., Fox, D. J. Gaussian 09, Revision A.02; Gaussian Inc 2016 Wallingford CT.

[50] J. Wang, W. Wang, P.A. Kollman, D.A. Case, Automatic atom type and bond type perception in molecular mechanical calculations, J. Mol. Graph. Model. 25 (2) (2006) 247–260.

[51] J.C. Shelley, A. Cholleti, L.L. Frye, J.R. Greenwood, M.R. Timlin, M. Uchimaya, Epik: a software program for pK(a) prediction and protonation state generation for drug-like molecules, J. Comput. Aided Mol. Des. 21 (12) (2007) 681–691.

[52] Schrödinger *Maestro*, Schrödinger: New York, NY, 2019.

[53] D.A. Case, I.Y. Ben-Shalom, S.R. Brozell, D.S. Cerutti, T.E. Cheatham III, V.W. D. Cruzeiro, T.A. Darden, R.E. Duke, D. Ghoreishi, M.K. Gilson, H. Gohlke, A. W. Goetz, D. Greene, R. Harris, N. Homeyer, S. Izadi, A. Kovalenko, T. Kurtzman, T. S. Lee, S. LeGrand, P. Li, C. Lin, J. Liu, T. Luchko, R. Luo, D.J. Mermelstein, K. M. Merz, Y. Miao, G. Monard, C. Nguyen, H. Nguyen, I. Omelyan, A. Onufriev, F. Pan, R. Qi, D.R. Roe, A. Roitberg, C. Sagui, S. Schott-Verdugo, J. Shen, C. L. Simmerling, J. Smith, R. Salomon-Ferrer, J. Swails, R.C. Walker, J. Wang, H. Wei, R.M. Wolf, X. Wu, L. Xiao, D.M. York, P.A. Kollman, AMBER, University of California, San Francisco, 2021.

[54] D.A. Case, T.E. Cheatham III, T. Darden, H. Gohlke, R. Luo, K.M. Merz Jr., A. Onufriev, C. Simmerling, B. Wang, R.J. Woods, The Amber biomolecular simulation programs, J. Comput. Chem. 26 (16) (2005) 1668–1688.

[55] R. Salomon-Ferrer, A.W. Götz, D. Poole, S. Le Grand, R. Walker, C., Routine Microsecond Molecular Dynamics Simulations with AMBER on GPUs. 2. Explicit Solvent Particle Mesh Ewald, J. Chem. Theory Comput. 9 (9) (2013) 3878–3888.

[56] S. Le Grand, A.W. Götz, R.C. Walker, SPFP: Speed without compromise—A mixed precision model for GPU accelerated molecular dynamics simulations, Comput. Phys. Commun. 184 (2) (2013) 374–380.

[57] J. Wang, R.M. Wolf, J.W. Caldwell, P.A. Kollman, D.A. Case, Development and testing of a general amber force field, J. Comput. Chem. 25 (9) (2004) 1157–1174.

[58] L. Martínez, R. Andrade, E.G. Birgin, J.M. Martínez, PACKMOL: A package for building initial configurations for molecular dynamics simulations, J. Comput. Chem. 30 (13) (2009) 2157–2164.

[59] T. Darden, D. York, L. Pedersen, Particle mesh Ewald: An N·log(N) method for Ewald sums in large systems, J. Chem. Phys. 98 (12) (1993) 10089–10092.

[60] J.-P. Ryckaert, G. Ciccotti, H.J.C. Berendsen, Numerical integration of the cartesian equations of motion of a system with constraints: molecular dynamics of n-alkanes, J. Comput. Phys. 23 (3) (1977) 327–341.

[61] Nguyen, H.; Roe, D. R.; Swails, J.; Case, D. A. PYTRAJ: Interactive data analysis for molecular dynamics simulations, 2016.

[62] D.R. Roe, T.E. Cheatham, PTRAJ and CPPTRAJ: Software for Processing and Analysis of Molecular Dynamics Trajectory Data, J. Chem. Theory Comput. 9 (7) (2013) 3084–3095.

[63] J. Srinivasan, T.E. Cheatham, P. Cieplak, P.A. Kollman, D.A. Case, Continuum Solvent Studies of the Stability of DNA, RNA, and Phosphoramidate−DNA Helices, J. Am. Chem. Soc. 120 (37) (1998) 9401–9409.

[64] P.A. Kollman, I. Massova, C. Reyes, B. Kuhn, S. Huo, L. Chong, M. Lee, T. Lee, Y. Duan, W. Wang, O. Donini, P. Cieplak, J. Srinivasan, D.A. Case, T.E. Cheatham, Calculating Structures and Free Energies of Complex Molecules: Combining Molecular Mechanics and Continuum Models, Acc. Chem. Res. 33 (12) (2000) 889–897.
[65] I. Massova, P.A. Kollman, Combined molecular mechanical and continuum solvent approach (MM-PBSA/GBSA) to predict ligand binding, Perspect. Drug Discov. Des. 18 (1) (2000) 113–135.
[66] N. Homeyer, H. Gohlke, Free Energy Calculations by the Molecular Mechanics Poisson−Boltzmann Surface Area Method, Mol. Inform. 31 (2) (2012) 114–122.
[67] D.A. Case, Normal mode analysis of protein dynamics, Curr. Opin. Struct. Biol. 4 (2) (1994) 285–290.
[68] B.R. Miller, T.D. McGee, J.M. Swails, N. Homeyer, H. Gohlke, A.E. Roitberg, MMPBSA.py: An Efficient Program for End-State Free Energy Calculations, J. Chem. Theory Comput. 8 (9) (2012) 3314–3321.
[69] B. Honig, A. Nicholls, Classical electrostatics in biology and chemistry, Science 268 (5214) (1995) 1144–1149.
[70] M.K. Gilson, K.A. Sharp, B.H. Honig, Calculating the electrostatic potential of molecules in solution: Method and error assessment, J. Comput. Chem. 9 (4) (1988) 327–335.
[71] C. Tan, Y.-H. Tan, R. Luo, Implicit Nonpolar Solvent Models, J. Phys. Chem. B 111 (42) (2007) 12263–12274.
[72] D.A. McQuarrie, Statistical Mechanics, 2nd ed., University Science Books, 2000.
[73] G.D. Hawkins, C.J. Cramer, D.G. Truhlar, Pairwise solute descreening of solute charges from a dielectric medium, Chem. Phys. Lett. 246 (1) (1995) 122–129.
[74] G.D. Hawkins, C.J. Cramer, D.G. Truhlar, Parametrized Models of Aqueous Free Energies of Solvation Based on Pairwise Descreening of Solute Atomic Charges from a Dielectric Medium, J. Phys. Chem. 100 (51) (1996) 19824–19839.
[75] J. Janin, For Guldberg and Waage, with love and cratic entropy, Proteins Struct. Funct. Bioinf. 24 (4) (1996) i–ii.
[76] M.K. Gilson, J.A. Given, B.L. Bush, J.A. McCammon, The statistical-thermodynamic basis for computation of binding affinities: a critical review, Biophys. J. 72 (3) (1997) 1047–1069.
[77] H. Luo, K. Sharp, On the calculation of absolute macromolecular binding free energies, PNAS 99 (16) (2002) 10399–10404.
[78] P. Narang, T.E. de Oliveira, P. Venkatesu, P.A. Netz, The role of osmolytes in the temperature-triggered conformational transition of poly(N-vinylcaprolactam): an experimental and computational study, Phys. Chem. Chem. Phys. 22 (9) (2020) 5301–5313.
[79] R. Umapathi, P. Venkatesu, Assessing the efficiency of imidazolium-based ionic liquids on the phase behavior of a synthetic biomedical thermoresponsive polymer, J. Colloid Interface Sci. 511 (2018) 174–183.
[80] H. Fan, L. Wang, X. Feng, Y. Bu, D. Wu, Z. Jin, Supramolecular Hydrogel Formation Based on Tannic Acid, Macromolecules 50 (2) (2017) 666–676.